

**Form for reporting suspicion of research misconduct or questionable research practices to the Practice Committee at the University of Copenhagen.**



**Complainant:**

Full name:	
Address:	
Postal code:	City:
Telephone:	Civil registration number/central business register:
Email:	

**Respondent:**

Full name:	
Address:	
Postal code:	City:
Telephone:	Civil registration number:
Email:	

**Case:****Complainant's claim(s):**

Please specify which specific acts, omissions etc. are claimed to be research misconduct or questionable research practices.

**The subject of the complaint:**

Please specify whether the complaint concerns a particular product (e.g. a text or a figure). If so, the product must be attached as an appendix to this complaint.

If the complaint concerns communication, a course of events, etc., please attach evidence of the most essential parts hereof, e.g. in the form of emails, protocols, records, minutes, etc.

**Presentation of the case:**

With reference to the evidence submitted, please describe the main events in the case necessary to understand the complaint.

**Complainant's argument(s):**

In as much detail as possible, please state the arguments and evidence that support the claim. For instance, claims of plagiarism must be accompanied by a precise reference to the relevant pages/sections/lines.

**Appendices:**

In general, please document all information by appendices.  
 Appendices must be attached to the complaint according to date and must be numbered consecutively as "Appendix 1", "Appendix 2" etc.

<b>Appendix no.:</b>	<b>Appendix title:</b>
Appendix 1	
Appendix 2	
Appendix 3	
Appendix 4	
Appendix 5	
Appendix 6	
Appendix 7	
Appendix 8	
Appendix 9	
Appendix 10	
Appendix 11	
Appendix 12	
Appendix 13	
Appendix 14	
Appendix 15	
Appendix 16	
Appendix 17	
Appendix 18	
Appendix 19	
Appendix 20	

**Complainant's signature:**

Place and date:	Signature:
-----------------	------------

**Specifically on plagiarism:**

If the complaint concerns suspicions of plagiarism in particular, the scientific product must be attached, i.e. the text (e.g. a published article) claimed to contain plagiarized content.

In this text, highlight sections claimed to be plagiarized. Every highlight must include a note indicating what source has been plagiarized. Both highlights and notes can be made using standard features of Acrobat Reader. Other tools can also be used, e.g. PDF Annotator, Bluefire Reader and GoodReader.

Likewise, you must attach the plagiarized text and highlight the places where the plagiarized text can be found in the scientific product.

Attach all texts relevant to the complaint in their entirety as PDF files and if possible with OCR functionality (optical character recognition).

If the complaint involves more than one case of plagiarism, it should contain precise information on each case.

**Specifically on co-authoring and other credit:**

If the complaint of questionable research practices concerns lack of credit in a product (e.g. in an article) the product must be attached, i.e. the text (e.g. a published article) claimed lack credit.

If the complaint concerns refused co-authorship, please attach evidence that you have contributed substantially to the research that the product is based on.

If the complaint concerns a claim that you have not been appropriately acknowledged, e.g. under acknowledgement(s), please attach evidence that you have performed important work or made an intellectual contribution that has influenced the research. Please refer to section 4(1) in The Danish Code of Conduct for Research Integrity.

To present the evidence necessary to prove lack of credit you may have to present emails showing the research project's development and any potential contracts agreed upon by between you and other researchers.

**Submission of complaint:**

Fill in the form and with appendices attached, submit it to the Practice Committee's secretariat in e.g. one of the following ways:

- By e-boks (Danish government secure electronic mail) to: University of Copenhagen, CVR No.: 29 97 98 12, attn.: The Practice Committee's secretariat
- By secure email to: [rektorsekretariatet@adm.ku.dk](mailto:rektorsekretariatet@adm.ku.dk), attn.: The Practice Committee's secretariat
- By regular mail to: Rector's Office, Nørregade 10, PO BOX 2177, 1077 København K, attn.: The Practice Committee's secretariat

**Additional information about the Practice Committee:**

See information about the Practice Committee, responsible research practices at the University of Copenhagen and case administration in the Practice Committee on the website at

[www.praksisudvalget.ku.dk/english](http://www.praksisudvalget.ku.dk/english).

**The Practice Committee's handling of personal data:**

The University of Copenhagen is the data controller of the personal data, which the Practice Committee receives and obtains in connection with cases, which the Practice Committee manages and processes under act no. 383 of 26 April 2017 on research misconduct etc<sup>1</sup>.

The personal data are processed by the Practice Committee according to the rules of the data protection regulation article 6(1) (c) and (e).

The Practice Committee at the University of Copenhagen will obtain the information necessary for proceeding the case. This will usually be information on civil registration number, name, address, employment, publications, research, education and email address.

This means that the Practice Committee at the University of Copenhagen can register, process and exchange information with the Danish Committee on Research Misconduct and with the parties of the case in order to consider the case under the legislation. This also means that the parties to cases before the Practice Committee generally are entitled to obtain access to the Practice Committee's information processed about the party itself and have the right to make objection against that personal information is processed. Contact information of the Practice Committee's secretariat is stated above.

You can read more about the Practice Committee's handling of personal data in [the University of Copenhagen's general policy on information security](#).

The University of Copenhagen has a Data Protection Officer, whom the parties of the cases before the Practice Committee can contact if there are questions regarding the processing of personal data. You can contact the Data Protection Officer on [dpo@adm.ku.dk](mailto:dpo@adm.ku.dk)

Complaints about the Practice Committee's processing of personal data please contact the Data Protection Agency on [dt@datatilsynet.dk](mailto:dt@datatilsynet.dk)

---

<sup>1</sup> [English translation of the Executive Order on the Danish Committees on Scientific Dishonesty \(only the Danish document has legal validity\)](#)

# Editorial Expression of Concern

On 27 March 2020, *Science* published the Research Article “Flux-induced topological superconductivity in full-shell nanowires” by S. Vaitiekėnas *et al.* (1). Pursuant to a reader request, the authors released additional data—archived at Zenodo (2)—taken in association with the project that led to their paper. After the release of the additional data, two readers expressed a joint concern that the tunneling spectroscopy data published in the original paper are not representative of the entirety of the data released in association with this project. While we await the outcome of a full investigation commenced by the authors’ academic institution (Niels Bohr Institute, University of Copenhagen), we are alerting our readers to this concern.

**H. Holden Thorp**  
Editor-in-Chief

## REFERENCES AND NOTES

1. S. Vaitiekėnas *et al.*, *Science* **367**, eaav3392 (2020).
2. S. Vaitiekėnas *et al.*, “Replication data for: Flux-induced topological superconductivity in full-shell nanowires,” Zenodo (2019); <http://doi.org/10.5281/zenodo.4263106>.

## RESEARCH ARTICLE SUMMARY

## TOPOLOGICAL MATTER

## Flux-induced topological superconductivity in full-shell nanowires

S. Vaitiekėnas, G. W. Winkler, B. van Heck, T. Karzig, M.-T. Deng, K. Flensberg, L. I. Glazman, C. Nayak, P. Krogstrup, R. M. Lutchyn\*, C. M. Marcus\*

**INTRODUCTION:** Majorana zero modes (MZMs) localized at the ends of one-dimensional topological superconductors are promising candidates for fault-tolerant quantum computing. One approach among the proposals to realize MZMs—based on semiconducting nanowires with strong spin-orbit coupling subject to a Zeeman field and superconducting proximity effect—has received considerable attention, yielding increasingly compelling experimental results over the past few years. An alternative route to MZMs aims to create vortices in topological superconductors, for instance, by coupling a vortex in a conventional superconductor to a topological insulator.

**RATIONALE:** We introduce a conceptually distinct approach to generating MZMs by threading magnetic flux through a superconducting shell fully surrounding a spin-orbit-coupled semiconducting nanowire core; this approach contains elements of both the proximitized-wire and vortex schemes. We show experimentally and theoretically that the winding of

the superconducting phase around the shell induced by the applied flux gives rise to MZMs at the ends of the wire. The topological phase sets in at relatively low magnetic fields, is controlled by moving from zero to one phase twist around the superconducting shell, and does not require a large  $g$  factor in the semiconductor, which broadens the landscape of candidate materials.

**RESULTS:** In the destructive Little-Parks regime, the modulation of critical temperature with flux applied along the hybrid nanowire results in a sequence of lobes with reentrant superconductivity. Each lobe is associated with a quantized number of twists of the superconducting phase in the shell, determined by the external field. The result is a series of topologically locked boundary conditions for the proximity effect in the semiconducting core, with a dramatic effect on the subgap density of states.

Tunneling into the core in the zeroth superconducting lobe, around zero flux, we mea-

sure a hard proximity-induced gap with no subgap features. In the superconducting regions around one quantum of applied flux,  $\Phi_0 = h/2e$ , corresponding to phase twists of  $\pm 2\pi$  in the shell, tunneling spectra into the core show stable zero-bias peaks, indicating a discrete subgap state fixed at zero energy.

Theoretically, we find that a Rashba field arising from the breaking of local radial inversion symmetry at the semiconductor-superconductor interface, along with  $2\pi$ -phase twists in the boundary condition, can

## ON OUR WEBSITE

Read the full article at <http://dx.doi.org/10.1126/science.aav3392>

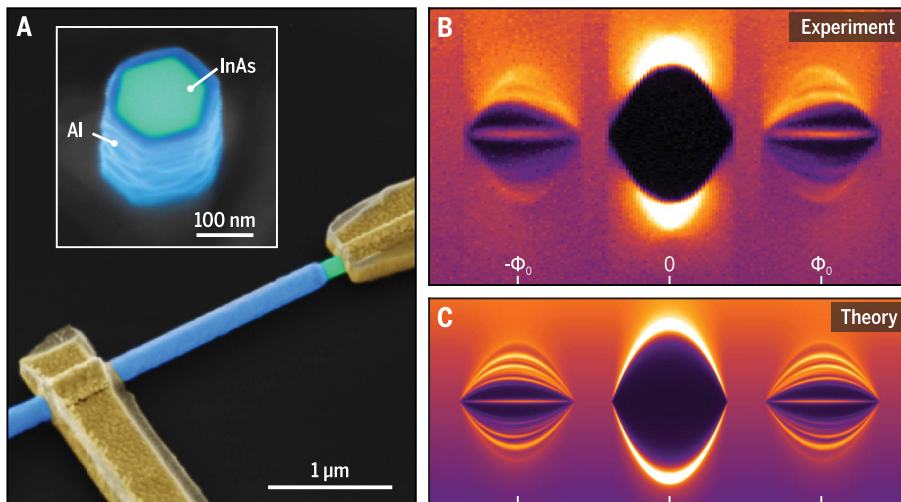
induce a topological state supporting MZMs. We calculate the topological phase diagram of the system as a function of Rashba spin-orbit coupling, radius of the semiconducting core, and band

bending at the superconductor-semiconductor interface. Our analysis shows that topological superconductivity extends in a reasonably large portion of the parameter space. Transport simulations of the tunneling conductance in the presence of MZMs qualitatively reproduce the experimental data in the entire voltage-bias range.

We obtain further experimental evidence that the zero-energy states are delocalized at wire ends by investigating Coulomb blockade conductance peaks in full-shell wire islands of various lengths. In the zeroth lobe, Coulomb blockade peaks show  $2e$  spacing; in the first lobe, peak spacings are roughly  $1e$ -periodic, with slight even-odd alternation that vanishes exponentially with island length, consistent with overlapping Majorana modes at the two ends of the Coulomb island. The exponential dependence on length, as well as incompatibility with a power-law dependence, provides compelling evidence that MZMs reside at the ends of the hybrid islands.

**CONCLUSION:** While being of similar simplicity and practical feasibility as the original nanowire proposals with a partial shell coverage, full-shell nanowires provide several key advantages. The modest magnetic field requirements, protection of the semiconducting core from surface defects, and locked phase winding in discrete lobes together suggest a relatively easy route to creating and controlling MZMs in hybrid materials. Our findings open the possibility of studying an interplay of mesoscopic and topological physics in this system. ■

The list of author affiliations is available in the full article online.  
\*Corresponding author. Email: [rolutchy@microsoft.com](mailto:rolutchy@microsoft.com) (R.M.L.); [chmarcus@microsoft.com](mailto:chmarcus@microsoft.com) (C.M.M.)  
Cite this article as S. Vaitiekėnas et al., *Science* 367, eaav3392 (2020). DOI: 10.1126/science.aav3392



**Majorana fingerprints in full-shell nanowires.** (A) Colorized electron micrograph of a tunneling device composed of a hybrid nanowire with hexagonal semiconducting core and full superconducting shell. (B) Tunneling conductance (color) into the core as a function of applied flux (horizontal axis) and source-drain voltage (vertical axis) reveals a hard induced superconducting gap near zero applied flux and a gapped region with a discrete zero-energy state around one applied flux quantum,  $\Phi_0$ . (C) Realistic transport simulations in the presence of MZMs reproduce key features of the experimental data.

## RESEARCH ARTICLE

## TOPOLOGICAL MATTER

## Flux-induced topological superconductivity in full-shell nanowires

S. Vaitiekėnas<sup>1</sup>, G. W. Winkler<sup>2</sup>, B. van Heck<sup>2</sup>, T. Karzig<sup>2</sup>, M.-T. Deng<sup>1</sup>, K. Flensberg<sup>1</sup>, L. I. Glazman<sup>3</sup>, C. Nayak<sup>2</sup>, P. Krogstrup<sup>1</sup>, R. M. Lutchyn<sup>2\*</sup>, C. M. Marcus<sup>1\*</sup>

Hybrid semiconductor-superconductor nanowires have emerged as a promising platform for realizing topological superconductivity (TSC). Here, we present a route to TSC using magnetic flux applied to a full superconducting shell surrounding a semiconducting nanowire core. Tunneling into the core reveals a hard induced gap near zero applied flux, corresponding to zero phase winding, and a gapped region with a discrete zero-energy state around one applied flux quantum, corresponding to  $2\pi$  phase winding. Theoretical analysis indicates that the winding of the superconducting phase can induce a transition to a topological phase supporting Majorana zero modes. Measured Coulomb blockade peak spacing around one flux quantum shows a length dependence that is consistent with the existence of Majorana modes at the ends of the nanowire.

Majorana zero modes (MZMs) at the ends of one-dimensional topological superconductors are expected to exhibit nontrivial braiding statistics (1–3), opening a path toward topologically protected quantum computing (4, 5). Among the proposals to realize MZMs, an approach (6, 7) based on semiconducting nanowires with strong spin-orbit coupling subject to a Zeeman field and superconducting proximity effect has received particular attention, yielding compelling experimental signatures (8–12). An alternative route to MZMs aims to create vortices in spinless superconductors by various means: coupling a vortex in a conventional superconductor to a topological insulator (13–17) or conventional semiconductor (18, 19), using doped topological insulators (20), using iron-based superconductors (21), or using vortices in exotic quantum Hall analogs of spinless superconductors (22).

Here, we show both experimental and theoretical results suggesting that a hybrid nanowire consisting of a full superconducting (aluminum) shell surrounding a semiconducting (indium arsenide) core can be driven into a topological phase that supports MZMs at the wire ends by a flux-induced winding of the superconducting phase. This approach contains elements of both proximitized-wire schemes (6, 7) and vortex-based schemes (1, 13) for creating MZMs. The topological phase sets in at relatively low magnetic fields ( $\sim 0.1$  T), is controlled discretely by moving from zero to

one phase twist around the superconducting shell, and does not require a large  $g$  factor in the semiconductor, which broadens the landscape of candidate materials.

Although it is known that well-chosen superconducting phase differences can be used to break time-reversal symmetry and localize MZMs in semiconducting heterostructures (23–28), the corresponding realizations typically require careful tuning of the fluxes. In contrast, vortices in a full-shell wire provide a naturally quantized means of controlling the superconducting phase. In the destructive Little-Parks regime (29, 30), the modulation of critical current and temperature with flux applied along the hybrid nanowire results in a sequence of lobes with reentrant superconductivity (31, 32). Each lobe is associated with a quantized number of twists of the superconducting phase (33), determined by the external field so that the free energy of the superconducting shell is minimized. The result is a series of topologically locked boundary conditions for the proximity effect in the semiconducting core, with a drastic effect on the subgap density of states.

Our measurements reveal that tunneling into the core in the zeroth superconducting lobe, around zero flux, yields a hard proximity-induced gap with no subgap features. In the superconducting regions around one quantum of applied flux, corresponding to phase twists of  $\pm 2\pi$  in the shell, tunneling spectra into the core show stable zero-bias peaks, indicating a discrete subgap state fixed at zero energy.

Theoretically, we find that a Rashba field arising from the breaking of local radial inversion symmetry at the semiconductor-superconductor interface (34–36), along with  $2\pi$ -phase twists in the boundary condition,

can induce a topological state supporting MZMs. We calculate the topological phase diagram of the system as a function of various parameters, such as Rashba spin-orbit coupling, radius of the semiconducting core, and band bending at the semiconductor-superconductor interface (34–36). Our analysis shows that topological superconductivity extends for a reasonably large portion of the parameter space. Transport simulations of the tunneling conductance in the presence of MZMs qualitatively reproduce the experimental data in the entire voltage-bias range.

We obtain further experimental evidence that the zero-energy states are localized at wire ends by investigating Coulomb blockade conductance peaks in full-shell wire islands of various lengths. In the zeroth lobe, Coulomb blockade peaks show  $2e$  spacing, indicating Cooper-pair tunneling and an induced gap exceeding the island charging energy. In the first lobe, peak spacings are roughly  $1e$ -periodic, with a slight even-odd alternation that vanishes exponentially with island length, consistent with overlapping Majorana modes at the two ends of the Coulomb island, as investigated previously (10, 37). The exponential dependence on length and the incompatibility with a power-law dependence strongly suggest that MZMs reside at the ends of the hybrid islands.

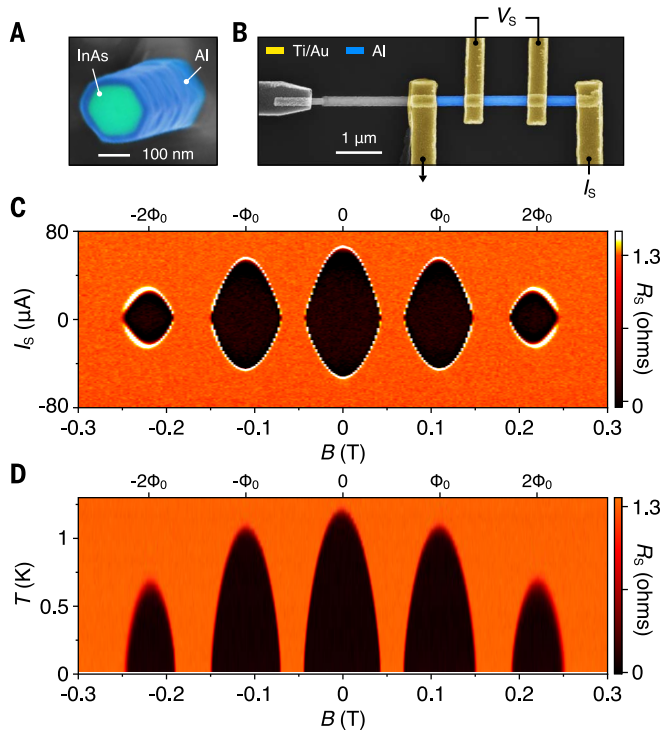
## Device description

InAs nanowires were grown by the vapor-liquid-solid method using molecular beam epitaxy. The nanowires had a hexagonal cross section with maximum diameter  $D = 130$  nm. A 30-nm epitaxial Al layer was grown while rotating the sample, yielding a fully enclosing shell (Fig. 1A) (38). Devices were fabricated using electron beam lithography. Standard alternating current (ac) lock-in measurements were carried out in a dilution refrigerator with a base temperature of 20 mK. Magnetic field was applied parallel to the nanowire using a three-axis vector magnet. Two device geometries, measured in three devices each, showed similar results. Data from two representative devices are reported in the main text: device 1 was used for four-probe measurements of the shell (Fig. 1B) and tunneling spectroscopy of the core (Fig. 2A); device 2 comprised six Coulomb islands of different lengths fabricated on a single nanowire, each with separate ohmic contacts, two side gates to trim tunnel barriers, and a plunger gate to change occupancy (see the Coulomb blockade spectroscopy section). Supporting data from three additional tunneling devices, one of which has a thinner shell, and two Coulomb-blockaded devices are presented in Figs. S5 to S7, S21, and S22 (39). For more detailed description of the wire growth, device fabrication, and

<sup>1</sup>Center for Quantum Devices and Microsoft Quantum Lab—Copenhagen, Niels Bohr Institute, University of Copenhagen, 2100 Copenhagen, Denmark. <sup>2</sup>Microsoft Quantum, Microsoft Station Q, University of California, Santa Barbara, Santa Barbara, CA 93106, USA. <sup>3</sup>Departments of Physics and Applied Physics, Yale University, New Haven, CT 06520, USA. \*Corresponding author. Email: rolutchy@microsoft.com (R.M.L.); chmarcus@microsoft.com (C.M.M.)

### Fig. 1. Destructive Little-Parks regime in full-shell nanowire device.

(A) Colorized material-sensitive electron micrograph of InAs-Al hybrid nanowire. Hexagonal InAs core (maximum diameter: 130 nm) with 30-nm full-shell epitaxial Al. (B) Micrograph of device 1, colorized to highlight four-probe measurement setup. (C) Differential resistance of the Al shell,  $R_S$ , as a function of current bias,  $I_S$ , and axial magnetic field,  $B$ , measured at 20 mK. Top axis shows flux,  $BA_{\text{wire}}$ , in units of the flux quantum  $\Phi_0 = h/2e$ , with Planck constant  $h$  and electric charge  $e$ . Superconducting lobes are separated by destructive regions near odd half-integer flux quanta. (D) Temperature evolution of  $R_S$  as a function of  $B$  measured around  $I_S = 0$ .  $R_S$  equals the normal-state resistance in all destructive regimes.



measurement techniques, see the Materials and methods section.

Differential resistance of the shell,  $R_S = dV_S/dI_S$ , measured for device 1 as a function of bias current,  $I_S$ , and axial magnetic field,  $B$ , showed a lobe pattern characteristic of the destructive regime (Fig. 1C) with a maximum switching current of 70  $\mu\text{A}$  at  $B = 0$ , the center of the zeroth lobe. Between the zeroth and first lobes, supercurrent vanished at  $|B| = 45$  mT, reemerged at 70 mT, and had a maximum near the center of the first lobe, at  $|B| = 110$  mT. A second lobe with smaller critical current was also observed, but a third lobe was not observed.

Temperature dependence of  $R_S$  around zero bias yielded a reentrant phase diagram with superconducting regions separated by destructive regions with temperature-independent normal-state resistance  $R_S^{(N)} = 1.3$  ohms (Fig. 1D).  $R_S^{(N)}$  and shell dimensions from Fig. 1A yield a Drude mean free path of  $l = 19$  nm. The dirty-limit shell coherence length (33, 40)

$$\xi_S = \sqrt{\frac{\pi \hbar v_F l}{24 k_B T_C}} \quad (1)$$

can then be found using the zero-field critical temperature  $T_C = 1.2$  K from Fig. 1D and Fermi velocity of Al,  $v_F = 2 \times 10^6$  m/s (41), with reduced Planck constant  $\hbar$  and Boltzmann constant  $k_B$ , yielding  $\xi_S = 180$  nm. The same values

for  $\xi_S$  are found using the onset of the first destructive regime (42).

#### Tunneling spectroscopy

Differential conductance,  $dI/dV$ , as a function of source-drain voltage,  $V$ , measured in the tunneling regime as a probe of the local density of states at the end of the nanowire is shown in Fig. 2. The Al shell was removed at the end of the wire, and the tunnel barrier was controlled by the global back-gate at voltage  $V_{\text{BG}}$ . At zero field, a hard superconducting gap was observed throughout the zeroth superconducting lobe (Fig. 2, B and D). Similar to the supercurrent measurements presented above, the superconducting gap in the core closed at  $|B| = 45$  mT and reopened at 70 mT, separated by a gapless destructive regime. Upon reopening, a narrow zero-bias conductance peak was observed throughout the first gapped lobe (Fig. 2, B and F). Several flux-dependent subgap states are also visible, separated from the zero-bias peak in the first lobe. These nonzero subgap states are analogs of Caroli-de Gennes-Matricon bound states (43), in this case confined at the metal-semiconductor interface rather than around a vortex core.

The first lobe persists to 150 mT, above which a second gapless destructive regime was observed. A second gapped lobe centered around  $|B| = 220$  mT then appeared, containing several subgap states away from zero energy, as shown in greater detail in (39). The

second lobe closes at 250 mT, above which only normal-state behavior was observed.

The dependence of tunneling spectra on back-gate voltage in the zeroth lobe is shown in Fig. 2C. In a weak tunneling regime, for  $V_{\text{BG}} < -1$  V, a hard gap was observed, with  $\Delta = 180$   $\mu\text{eV}$  (Fig. 2, C and D). For  $V_{\text{BG}} \sim -0.8$  V, as the tunneling barrier is decreased, the subgap conductance is enhanced owing to Andreev processes. The increase in conductance at  $V_{\text{BG}} \sim -1.2$  V is likely caused by a resonance in the barrier. In the first lobe, at  $B = 110$  mT, the sweep of  $V_{\text{BG}}$  showed a zero-energy state throughout the tunneling regime (Fig. 2E). The cut displayed in Fig. 2F shows a discrete zero-bias peak separated from other states by a softened gap, presumably owing to finite temperature and level broadening in the junction. As the tunnel barrier is opened, the zero-bias peak gradually evolves into a zero-bias dip. The increase of finite-bias conductance compared with zero-bias conductance as tunnel barrier decreases is in qualitative agreement with theory supporting MZMs (44), although the crossover from a peak to a dip occurs at lower conductance than expected. Additional line-cuts and the tunneling spectroscopy for the second lobe are shown in Figs. S3 and S4 (39). Several discontinuities in spectra occurred as  $V_{\text{BG}}$  was swept at the same gate voltages in Fig. 2, C and E, presumably because of gate-dependent charge motion in the barrier.

#### Modeling of topological phases

To better understand the origin of the zero-energy modes in the first lobe, we analyze theoretically a semiconducting nanowire covered by a superconducting shell. First, we present a toy model of a cylindrically symmetric full-shell wire (Fig. 3), highlighting the underlying mechanism of the topological phase appearance. Thereafter, we move on to simulations of realistic geometries (Figs. 4 and 5).

We assume that the semiconductor (InAs) has a large Rashba spin-orbit coupling owing to the local inversion symmetry breaking in the radial direction at the semiconductor-superconductor interface (corresponding to an electric field pointing along the radial direction at the superconductor-semiconductor interface). The system is subject to a magnetic field along the direction of the nanowire,  $\vec{B} = B\hat{z}$ . Using cylindrical coordinates and the symmetric gauge for the electromagnetic vector potential,  $\vec{A} = \frac{1}{2}(\vec{B} \times \vec{r})$ , the effective Hamiltonian for the semiconducting core can be written as

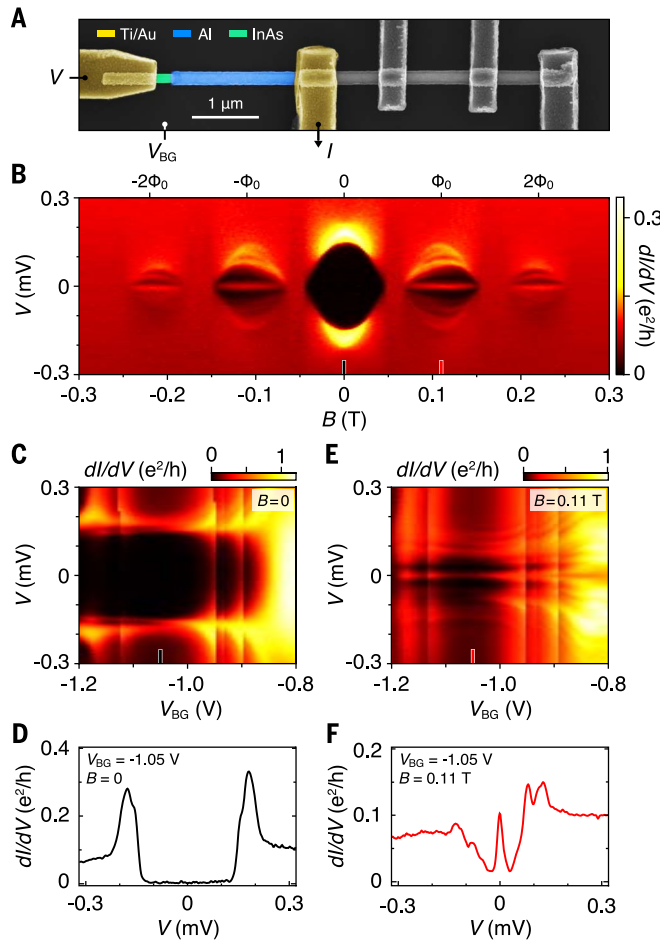
$$H_0 = \frac{(\vec{p} + eA_\varphi \hat{\varphi})^2}{2m^*} - \mu + \alpha \hat{r} \cdot [\vec{\sigma} \times (\vec{p} + eA_\varphi \hat{\varphi})] \quad (2)$$

Here, we use natural units ( $\hbar = 1$ ),  $\vec{p}$  is the electron momentum operator,  $e > 0$  the electric charge,  $m^*$  the effective mass,  $\mu$  is the chemical

**Fig. 2. Experimental tunneling spectrum.**

A hard gap is seen in the zeroth lobe, and a zero-bias peak in the first lobe.

(A) Micrograph of device 1, colorized to highlight tunneling spectroscopy setup. (B) Base temperature differential conductance,  $dI/dV$ , as a function of source-drain bias voltage,  $V$ , and axial field,  $B$ . The zeroth lobe shows a hard superconducting gap, the first lobes show a zero-bias peak, and the second lobes show nonzero subgap states. The lobes are separated by featureless normal-state spectra. (C) Zero-field conductance as a function of  $V$  and back-gate voltage,  $V_{BG}$ . (D) Line-cut of the conductance taken at  $B = 0$  and  $V_{BG} = -1.05$  V. (E and F) Similar to (C) and (D), measured in the first lobe at  $B = 110$  mT. Data shown are from two-terminal measurements, which include line resistances (see Materials and methods).



potential,  $\alpha$  the strength of the Rashba spin-orbit coupling, and  $\sigma_i$  are the spin-1/2 Pauli matrices.  $\hat{r}$ ,  $\hat{\phi}$ , and  $\hat{z}$  are the cylindrical unit vectors. For ease of presentation, we consider  $r$ -independent  $\mu$  and  $\alpha$  in our model, which may be viewed as averaged versions of the corresponding  $r$ -dependent quantities. The vector potential  $A_\phi = \Phi(r)/2\pi r$ ; where  $\Phi(r) = \pi B r^2$  is the flux threading the cross section at radius  $r$ . For simplicity, we neglect the Zeeman term caused by the small magnetic fields required in the experiment.

The superconducting shell (Al) induces superconducting correlations in the nanowire because of Andreev processes at the semiconductor-superconductor interface. If the tunnel coupling to the superconductor is weak, the induced pairing in the nanowire can be expressed as a local potential  $\Delta(\vec{r})$  (39). In the Nambu basis  $\Psi = (\psi_\uparrow, \psi_\downarrow, \psi_\uparrow^\dagger, -\psi_\downarrow^\dagger)$ , the Bogoliubov-de Gennes (BdG) Hamiltonian for the proximitized nanowire is then given by

$$H_{\text{BdG}} = \begin{bmatrix} H_0(\vec{A}) & \Delta(\vec{r}) \\ \Delta^*(\vec{r}) & -\sigma_y H_0(-\vec{A})^* \sigma_y \end{bmatrix} \quad (3)$$

We assume that the thickness of the shell is smaller than London penetration depth:

$R_3 - R_2 \ll \lambda_L$ . Therefore, the magnetic flux threading the shell is not quantized. However, the magnetic field induces a winding of the superconducting phase of the order parameter  $\Delta(\vec{r}) = \Delta(r)e^{-in\phi}$ , with  $\phi$  the angular coordinate and  $n \in \mathbb{Z}$  the winding number determined by the external magnetic flux.

We notice the following rotational symmetry of the BdG Hamiltonian:  $[J_z, H_{\text{BdG}}] = 0$  with  $J_z = -i\partial_\phi + \frac{1}{2}\sigma_z + \frac{1}{2}n\tau_z$ , where we introduced  $\tau_i$  matrices acting in Nambu space. Eigenstates of  $H_{\text{BdG}}$  can thus be labeled by a conserved quantum number  $m_J$ :  $\Psi_{m_J}(r, \phi, z) \propto e^{i(m_J - \frac{1}{2}\sigma_z - \frac{1}{2}n\tau_z)\phi} \Psi_{m_J}(r, z)$ . The wave function has to be single-valued, which imposes the following constraint on  $m_J$

$$m_J \in \begin{cases} \mathbb{Z} & n \text{ odd,} \\ \mathbb{Z} + \frac{1}{2} & n \text{ even} \end{cases} \quad (4)$$

Note that the particle-hole symmetry relates states with opposite energy and angular quantum number  $m_J$ , that is  $\mathcal{P}\Psi_{E, m_J} = \Psi_{-E, -m_J}$  with  $\mathcal{P} = \tau_y \sigma_y \mathcal{K}$ , where  $\mathcal{K}$  represents complex conjugation. Thus, the  $m_J = 0$  sector—allowed when the winding number  $n$  is odd—is special because it allows nondegenerate Majorana solutions at zero energy, as shown below.

The angular dependence of  $H_{\text{BdG}}$  can be eliminated via a unitary transformation  $U = \exp[-i(m_J - \frac{1}{2}\sigma_z - \frac{1}{2}n\tau_z)\phi]$ , namely  $\tilde{H}_{\text{BdG}} = UH_{\text{BdG}}U^\dagger$  where

$$\begin{aligned} \tilde{H}_{\text{BdG}} = & \left( \frac{p_z^2}{2m^*} + \frac{p_r^2}{2m^*} - \mu \right) \tau_z \\ & + \frac{1}{2m^*r^2} \left( m_J - \frac{1}{2}\sigma_z - \frac{1}{2}n\tau_z + eA_\phi r\tau_z \right)^2 \tau_z \\ & - \frac{\alpha}{r} \sigma_z \tau_z \left( m_J - \frac{1}{2}\sigma_z - \frac{1}{2}n\tau_z + eA_\phi r\tau_z \right) \\ & + \alpha p_z \sigma_y \tau_z + \Delta(r) \tau_x \end{aligned} \quad (5)$$

Here,  $p_r^2 = -\frac{1}{r}\partial_r r \partial_r$  and  $p_z = -i\partial_z$ . Although the spin-orbit coupling might, naively, be expected to average out, the nontrivial structure of  $m_J$  eigenvectors yields finite matrix elements proportional to the Rashba spin-orbit coupling.

Assuming that the electrons in the core are localized at the interface, we set  $R_1 \approx R_2$  (Fig. 3A). This approximation is motivated by the fact that there is an accumulation layer in certain semiconductor-superconductor heterostructures such as InAs-Al, as explained below. In this case, electrons in the semiconductor effectively form a thin-wall hollow cylinder, and only the lowest-energy radial mode in Eq. 5 needs to be considered. This allows for an analytical solution of the model. The effective Hamiltonian for the hollow-cylinder model reads

$$\begin{aligned} \tilde{H}_{m_J} = & \left[ \frac{p_z^2}{2m^*} - \mu_{m_J} \right] \tau_z + V_Z \sigma_z + A_{m_J} \\ & + C_{m_J} \sigma_z \tau_z + \alpha p_z \sigma_y \tau_z + \Delta \tau_x \end{aligned} \quad (6)$$

Here,  $\Delta \equiv \Delta(R_2)$  and the parameters  $\mu_{m_J}$  and  $V_Z$  correspond to the effective chemical potential and Zeeman energy.  $A_{m_J}$  and  $C_{m_J}$  represent the coupling of the generalized angular momentum  $J_z$  with magnetic field and electron spin, respectively. The effective parameters are defined as

$$\mu_{m_J} = \mu - \frac{1}{8m^*R_2^2} (4m_J^2 + 1 + \phi^2) - \frac{\alpha}{2R_2} \quad (7)$$

$$V_Z = \phi \left( \frac{1}{4m^*R_2^2} + \frac{\alpha}{2R_2} \right) \quad (8)$$

$$A_{m_J} = -\frac{\phi m_J}{2m^*R_2^2} \quad (9)$$

$$C_{m_J} = -m_J \left( \frac{1}{2m^*R_2^2} + \frac{\alpha}{R_2} \right) \quad (10)$$

with  $\phi = n - \Phi(R_2)/\Phi_0$ .

Equations 7 to 10 allow the identification of a topological phase in the  $m_J = 0$  sector of the

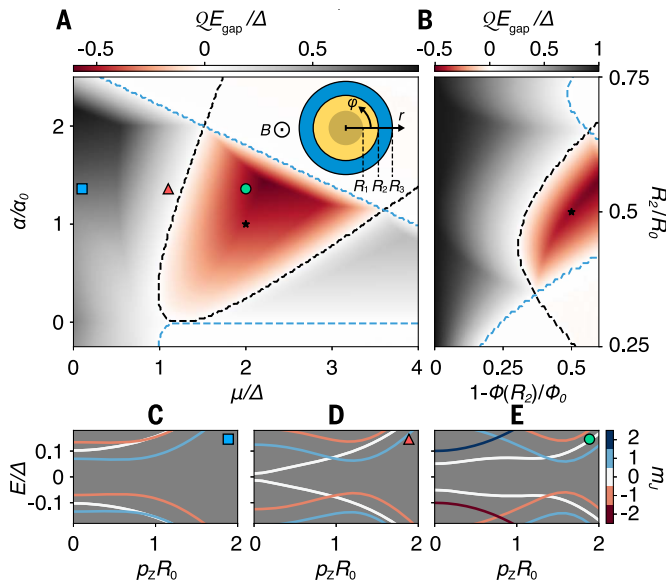


**Fig. 3. Topological phase diagram in a hollow-cylinder model.** (A) Bulk energy gap,  $E_g$ , as a function of chemical potential and spin-orbit coupling. The energy gap is multiplied by the topological index  $Q = \pm 1$ , so that red regions correspond to the gapped topological phase. The black dashed line denotes the boundary of the topological phase in the  $m_J = 0$  sector, according to Eq. 11, whereas the blue dashed lines denote the boundaries at which higher  $m_J$  sectors become gapless (39). Here,  $\Phi(R_2)/\Phi_0 = \frac{1}{2}$ ,  $R_1/R_0 = \frac{1}{2}$ . We define  $\alpha_0 = \sqrt{\Delta/2m^*}$  and  $R_0 = 1/\sqrt{2m^*}\Delta$ . For reference, using realistic parameters  $m^* = 0.026 m_e$  and  $\Delta = 0.2$  meV, one obtains  $\alpha_0 \approx 17$  meV·nm and  $R_0 \approx 85$  nm. Inset shows cross section of a semiconducting nanowire (yellow) with a full superconducting shell (blue), subject to a weak axial magnetic field  $B$ . The shaded yellow region with  $r < R_1$  indicates the possible presence of an insulating core in the semiconductor. (B) Bulk energy gap at fixed  $\mu/\Delta = 2$  and  $\alpha/\alpha_0 = 1$ , as indicated by a black star in (A), as a function of flux and  $R$ . (C to E) Band structures at the points indicated with colored square, triangle, and circle in (A), illustrating the closing and reopening of the bulk gap in the  $m_J = 0$  sector.

first lobe where  $n = 1$ . In this case,  $A_0 = 0$  and  $C_0 = 0$ , and Eq. 6 can be mapped to the Majorana nanowire model in (6, 7). Note that the effective Zeeman term has an orbital origin here and is present even when the  $g$  factor in the semiconductor is zero. Both  $\mu_0$  and  $V_Z$  can be tuned by the magnetic flux  $\Phi(R_2)$ , which may induce a topological phase transition. In the hollow-cylinder approximation,  $V_Z = 0$  when the core is penetrated by one flux quantum [ $\Phi(R_2) = \Phi_0$ ]. This regime corresponds to the trivial (s-wave) superconducting phase. However, a small deviation of the magnetic flux can drive the system into the topological superconducting phase (45). Indeed, the Zeeman and spin-orbit terms in Eq. 6 do not commute, and thus  $V_Z$  opens a gap in the spectrum at  $p_z = 0$ . At the topological quantum phase transition between the two phases, the gap in the  $m_J = 0$  sector

$$E_{\text{gap}}^{(0)} = \left| |V_Z| - \sqrt{\mu_0^2 + \Delta^2} \right| \quad (11)$$

closes. The resulting phase diagram is shown in Fig. 3, where the gap closing at the topological transition is indicated by black dashed

lines. Close to the transition, the quasiparticle spectrum in the  $m_J = 0$  sector is given by  $E(p_z) = \sqrt{(E_{\text{gap}}^{(0)})^2 + (vp_z)^2}$  with  $v = \alpha\Delta/\sqrt{\Delta^2 + \mu_0^2}$  and the corresponding topological coherence length  $\xi_T \sim v/E_{\text{gap}}^{(0)}$ .

A well-defined topological phase requires the quasiparticle bulk gap to be finite for all values of  $m_J$ . Owing to the angular symmetry of Eq. 6, different  $m_J$  sectors do not mix and, as a result, the condition for a finite gap in the  $m_J \neq 0$  sectors is  $\Delta^2 + (C_{m_J} - \mu_{m_J})^2 > (A_{m_J} + V_Z)^2$  (39). In general, the topological phase diagram can be obtained by calculating the topological index  $Q$  (2)

$$Q = \text{sign} \prod_{m_J \in Z} \left[ \Delta^2 + (C_{m_J} - \mu_{m_J})^2 - (A_{m_J} + V_Z)^2 \right] \quad (12)$$

where  $Q = 1$  and  $Q = -1$  correspond to trivial and topological phases, respectively. Thus, the topological phase supporting MZMs appears as a result of the change of  $Q$  in the  $m_J = 0$  sector. Figure 3 shows the topological phase diagram and energy gap of the hollow-cylinder

model determined by taking into account all  $m_J$  sectors.

The hollow-cylinder model provides conceptual understanding for the existence of the topological phase in full-shell nanowires. The model, however, is limited to small chemical potentials and a conserved angular momentum. For a direct comparison with the experiment, more realistic simulations extending to the regime with multiple radial modes are needed.

### Realistic simulations

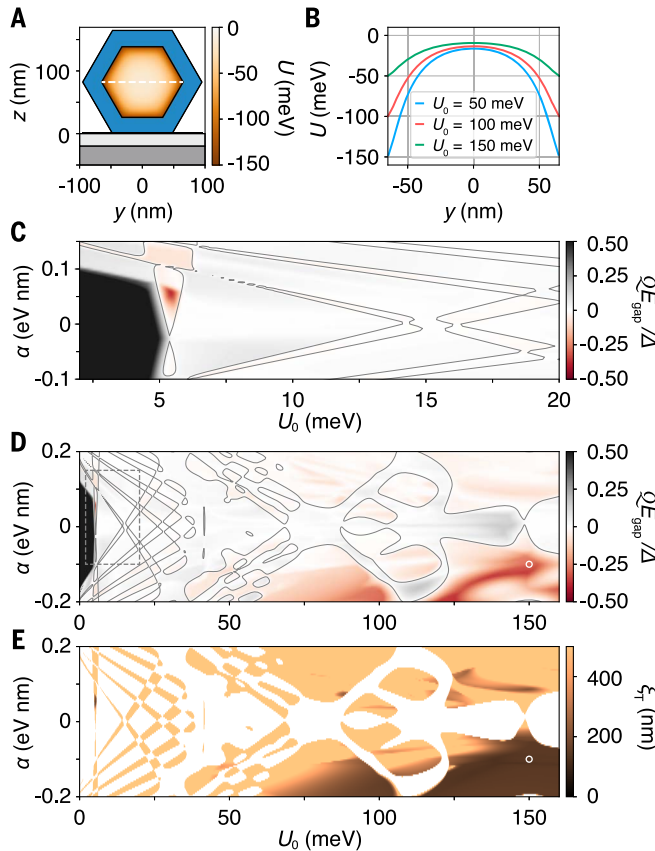
Recent advances in the modeling of semiconductor-superconductor hybrid structures have led to more accurate simulations of proximitized nanowires (34, 35, 46, 47). Here, the essence of our approach is to integrate out the superconductor into self-energy boundary conditions, as discussed in (39). This approximation allows for three-dimensional (3D) simulations of proximitized nanowires, including important effects such as self-consistent electrostatics and orbital magnetic field contribution (48).

We model a hexagonal InAs wire with 130 nm corner-to-corner diameter coated by a 30-nm-thick Al shell (Fig. 4A). The work function difference between InAs and Al leads to a band offset between the conduction band of InAs and the Fermi level of Al, resulting in an electron accumulation layer close to the interface (Fig. 4, A and B). This band offset is on the order of 100 meV (34, 35, 47, 49). The accumulation layer causes an intrinsic electric field for the electrons, resulting in Rashba spin-orbit coupling with the symmetry axis in an approximately radial direction (50, 51). The magnitude of  $\alpha$  has been experimentally determined to be in the range of 0.02 to 0.08 eV·nm (12).

Given the uncertainties, we calculate the topological phase diagram as a function of band offset,  $U_0$ , and the Rashba spin-orbit coupling,  $\alpha$  (52). The band offset controls the number of subbands in the nanowire as well as their population. For  $U_0 < 40$  meV, the system is in the single radial mode regime, and the phase diagram appears qualitatively similar to the hollow-cylinder model (Fig. 4, C and D). Around 5 meV there is a gapped topological phase that we identify with the  $m_J = 0$  angular sector, analogous to the hollow-cylinder model. In this  $U_0$  regime, apart from the  $m_J = 0$  sector, the topological phases have very small gaps. The vertical feature at  $U_0 \sim 40$  meV band offset in Fig. 3D corresponds to a second radial subband with  $m_J = 0$  crossing the Fermi level.

For  $U_0 > 40$  meV, the phase diagram becomes qualitatively different. Owing to the increased number of bands, the different topological phases hybridize and merge into extended topological regions (53, 54). Furthermore, as

**Fig. 4. Modeling the electrostatic potential and topological phase diagram.** (A) Schematic cross section of the wire superimposed with the simulated potential energy,  $U$ , in the semiconductor for band offset  $U_0 = 150$  meV. (B) Horizontal cuts of the potential in the wire for different band offsets. (C) Topological phase diagram of the full-shell nanowire in the first lobe at  $B = 0.124$  T as a function  $U_0$  and spin-orbit coupling,  $\alpha$ , close to the  $m_J = 0$  topological phase. The gray lines indicate a change of the sign of the Pfaffian,  $Q$ . (D) Topological phase diagram for the same set of parameters as in (C), over a large range of band offsets. (E) Topological coherence length,  $\xi_T$ , computed for the same  $U_0$  and  $\alpha$  ranges as in (D).



$U_0$  increases, the wave functions are pushed closer to the superconductor, leading to a stronger hybridization of the wave functions with Al. In this  $U_0$  regime, one finds extended topological regions with sizable gaps that make up a substantial fraction of the superconducting gap.

Mixing of different angular sectors, facilitated by the broken cylindrical symmetry that, in turn, is a consequence of the hexagonal cross section, lifts the restriction that the MZMs must have zero angular momentum ( $m_J = 0$ ). In the case of broken angular symmetry (as a result of disorder in superconductor or geometrical effects),  $m_J$  is not a good quantum number and the topological superconducting phase may also appear at even winding numbers [see (39) for the topological phase diagram in the second lobe].

In addition to the gap size, we also compute the topological coherence length,  $\xi_T$  (Fig. 4E), from the eigenvalue decomposition of the translation operator at zero energy (55). As expected, regions with a large gap also have a short coherence length. Because of the smaller Fermi velocity in the semiconductor, the topological coherence length can be smaller than the  $s$ -wave coherence length. We find that the shortest  $\xi_T$  is  $\sim 120$  nm, whereas the typical values for realistic spin-orbit coupling strength and band offset range from 140 to 200 nm.

Having established bulk properties, we numerically compute a 3D full-shell wire in a transport geometry. The corresponding longitudinal cross section of the simulated device is shown in Fig. 5A. After calculating the electrostatic potential of the 3D structure, we simulate the quantum transport using the Kwant and adaptive packages (56, 57). Here, we focus on a single point in the phase diagram with band offset of 150 meV and  $\alpha = -0.1$  eV-nm (see open white circle in Fig. 4, D and E). Results for other representative points can be found in (39).

Computed conductance,  $dI/dv$ , as a function of bias voltage,  $v$ , and magnetic field,  $B$ , is shown in Fig. 5B. The simulated back-gate voltage,  $v_{BG}$ , is chosen such that there is good visibility of states in the wire. As in the experimental observations in Fig. 2B, the zeroth lobe shows a hard gap with no subgap states. The first and second lobes, on the other hand, show multiple subgap states (58). The first lobe has a gap with a zero-bias peak owing to Majorana end states. The size of the gap is consistent with the bulk phase diagram in Fig. 4D. The second lobe has more subgap states and appears to be gapless.

The evolution of the simulated spectrum with the back-gate voltage in the topological phase is displayed in Fig. 5C. As expected, the bias voltages at which zero-bias peak and subgap states are visible is independent of  $v_{BG}$ , but the intensities of the states change.

Because the wire is fully covered by a superconducting shell, the effect of the back gate is completely screened inside the bulk of the wire and does not influence the topological phase or bulk states. When the tunnel-barrier height is decreased, for  $v_{BG} > -0.1$  V, the zero-bias peak transforms into a zero-bias dip, as expected in this regime. The transport simulation incorporates a small amount of dissipation (see Materials and methods), leading to a finite conductance background and a non-quantized zero-bias peak (Fig. 5D), which is qualitatively similar to the data in Fig. 2F.

### Coulomb blockade spectroscopy

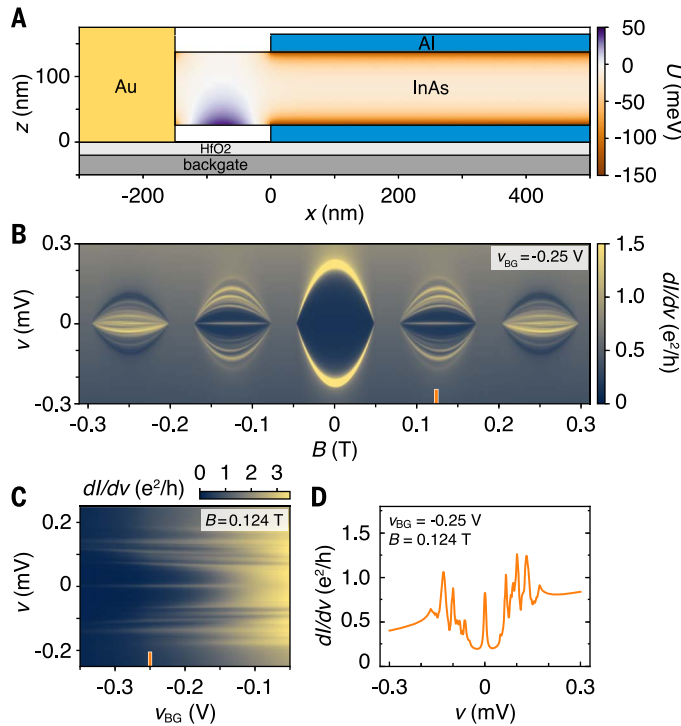
Tunneling spectra simulated around one applied flux quantum (Fig. 5) indicate a localized MZM at the end of the hybrid nanowire and agree well with the measurements (Fig. 2). The nature of the experimentally observed zero-bias peaks can be better understood from their length-dependent energy splitting. With this in mind, we experimentally investigate subgap-state hybridization, which can be measured using the spacing of Coulomb blockade conductance peaks in Coulomb islands as a function of island length (10, 37, 59, 60). The exponential length dependence of hybridization energy is a signature of MZMs localized at the opposite ends of the nanowire (61–63). We investigated full-shell islands over a range of device lengths from 210 to 970 nm, fabricated on a single nanowire, as shown in Fig. 6.

Zero-bias conductance as a function of plunger-gate voltage,  $V_G$ , and  $B$  for device 2 yielded a series of Coulomb blockade peaks for each segment, examples of which are shown in Fig. 6B. The corresponding average peak spacings,  $\delta\bar{V}$ , for even and odd Coulomb valleys as a function of  $B$  are shown in Fig. 6C. Around zero field, Coulomb blockade peaks with  $2e$  periodicity were found. These peaks split at  $\sim 40$  mT toward the high-field end of the zeroth superconducting lobe, as the superconducting gap decreased below the charging energy of the island. The peaks then became  $1e$ -periodic (within experimental sensitivity) around 55 mT and throughout the first destructive regime (see Fig. 1 for the onset of destructive regime). When superconductivity reappeared in the first lobe, the Coulomb peaks did not become spaced by  $2e$  again but instead showed nearly  $1e$  spacing with even-odd modulation. The 210-nm island showed a qualitatively similar even-odd peak spacing modulation, also in the second lobe. Unlike device 1, described in Fig. 2, the shortest island in device 2 showed a third superconducting lobe, which can be identified from the peak-height contrast in Fig. 6B. Coulomb blockade peaks were  $1e$ -periodic within experimental sensitivity throughout the third lobe.

Tunneling spectra at finite source-drain bias showed  $2e$  Coulomb diamonds around zero

### Fig. 5. Simulation of tunneling transport.

(A) Schematic side view of the normal-superconducting junction device superimposed with the simulated potential energy,  $U$ , in the semiconductor computed for band offset  $U_0 = 150$  meV and back-gate voltage  $v_{BG} = -0.25$  V. (B) Differential conductance  $dI/dv$  as a function of axial magnetic field,  $B$ , and bias voltage,  $v$ , simulated at  $v_{BG} = -0.3$  V,  $U_0 = 150$  meV, and spin-orbit coupling  $\alpha = -0.1$  eV·nm. (C) Differential conductance as a function of  $v_{BG}$  at  $B = 0.124$  T for the same  $U_0$  and  $\alpha$  as in (B). (D) Line-cut of the conductance at  $v_{BG} = -0.25$  V and  $B = 0.124$  T.



field (Fig. 6D) and nearly  $1e$  diamonds at  $B = 110$  mT, near the middle of the first lobe (Fig. 6E). The zero-field diamonds are indistinguishable from each other, showing a region of negative differential conductance associated with the onset of quasiparticle transport (64–66). In the first lobe (Fig. 6E), Coulomb diamonds alternate in size and symmetry, with degeneracy points showing sharp, gapped structure, indicating that the near-zero-energy state is discrete. Additional resonances at finite bias reflect excited discrete subgap states away from zero energy.

Coulomb peaks for two longer islands are shown in Fig. 7, A to E, with full datasets for other lengths shown in figs. S11 to S15 (39). All islands showed  $2e$ -periodic Coulomb peaks in the zeroth lobe and nearly  $1e$  spacing in the first lobe. Examining the 420 nm and 810 nm data in Fig. 7, A, C, and E, reveals that the mean difference between even and odd peak spacings in the first lobe decreased with increasing island length. To address this question quantitatively, we determine the lever arm,  $\eta$ , for each island independently to convert plunger gate voltages to chemical potentials on the islands, using the slopes of the Coulomb diamonds (10, 67). This allows the peak spacing differences (Fig. 7, B and D) to be converted to island-energy differences,  $A(L)$ , between even and odd occupations, as a function of device length,  $L$  [a detailed exemplar peak spacing analysis (fig. S17) is presented in (39)]. In the context of topological superconductivity, the

energy scale  $A(L)$  reflects the length-dependent hybridization energy of MZMs. Values for  $A(L)$  at  $B = 110$  mT, in the middle of the first lobe, spanning two orders of magnitude are shown in Fig. 7F. A fit to an exponential  $A = A_0 e^{-L/\xi}$  yields fit parameters  $A_0 = 105$   $\mu$ eV and  $\xi = 180$  nm. The data are well described by an exponential length dependence, implying that the low-energy modes are located at the ends of the wire, not bound to impurities or local potential fluctuations as expected for overlapping Majorana modes. The comparison of exponential and power-law fits (fig. S18) and the calculated length dependence that shows exponential decay only in topological regimes (fig. S24) are provided in (39). The measured  $\xi$  is consistent with the calculated  $\xi_T$  using realistic parameters.

Along with length-dependent even-odd peak spacing difference, we observe even-odd modulation in peak heights (Fig. 7E). A possible explanation of these phenomena was proposed in (68). Additionally, we find a complex alternating peak-height structure depending on magnetic field within the first lobe (Fig. 7E). Peak height modulation accompanying peak spacing modulation was observed previously (10, 59, 60).

To investigate how coherence length  $\xi$ , extracted from the exponential decrease of even-odd peak spacing with length, depends on the superconducting gap,  $\Delta$ , we examine peak spacing near the high-field edge of the first lobe,  $B = 140$  mT, where the gap is reduced to

$\Delta_{140} = 40$   $\mu$ eV, and shows no subgap features besides the zero-bias peak (fig. S19). At this reduced gap, we again find an exponential dependence on length, as well as incompatibility with a power law, now with  $\xi = 230$  nm. We observe that  $\xi_{140}/\xi_{110} = 230$  nm/180 nm  $\sim 1.3$  is consistent with simple scaling,  $\xi \propto \Delta^{-1}$  (not accounting for a field-dependent velocity). From the data shown in Fig. 2B and fig. S19,  $\delta_{110}/\Delta_{140} = 50$   $\mu$ eV/40  $\mu$ eV  $\sim 1.2$ , where  $\delta_{110}$  is the lowest nonzero subgap state, and  $\delta_{140} = \Delta_{140}$ . Both  $\xi_{110}$  and  $\xi_{140}$  are slightly smaller than the coherence length in the superconducting shell at corresponding B-field values:  $\xi_S(110$  mT)  $\sim 190$  nm and  $\xi_S(140$  mT)  $\sim 250$  nm, extracted from data in Fig. 1D using Eq. 1 and the corresponding values of  $T_C(B)$ . This discrepancy may be interpreted as resulting from the velocity renormalization in the semiconductor in the strong coupling limit (69–71).

### Outlook

In comparison to the original nanowire proposals with a partial shell coverage (6, 7), full-shell nanowires have similar simplicity and practical feasibility (38) but provide several key advantages. First, the topological transition in a full-shell wire is driven by the field-induced winding of the superconducting order parameter rather than by the Zeeman effect, so that, as demonstrated in the reported measurements, the required magnetic fields can be very low ( $\sim 0.1$  T). Therefore, the present proposal is compatible with conventional superconducting electronics and removes the need for a large  $g$  factor semiconductor, potentially expanding the landscape of candidate materials. Moreover, the full shell naturally protects the semiconductor from impurities and random surface doping, thus enabling a reproducible way of growing many wires with essentially identical electrostatic environments. Although full-shell wires do not allow for direct gating of the electron density in the semiconducting core, we demonstrated that, using a careful design of the wire properties—for example, by choosing the appropriate radius—it is possible to obtain wires that harbor MZMs at a predictable magnetic field. The modest magnetic field requirements, protection of the semiconducting core from surface defects, and locked phase winding in discrete lobes together suggest a distinct and relatively easy route to creating and controlling MZMs in hybrid materials. Our findings open a possibility to study an interplay of mesoscopic and topological physics in this system.

### Materials and methods

The hybrid nanowires used in this work were grown by molecular beam epitaxy on InAs (111)B substrate at 420°C. The growth was catalyzed by Au via the vapor-liquid-solid method. The nanowire growth was initiated

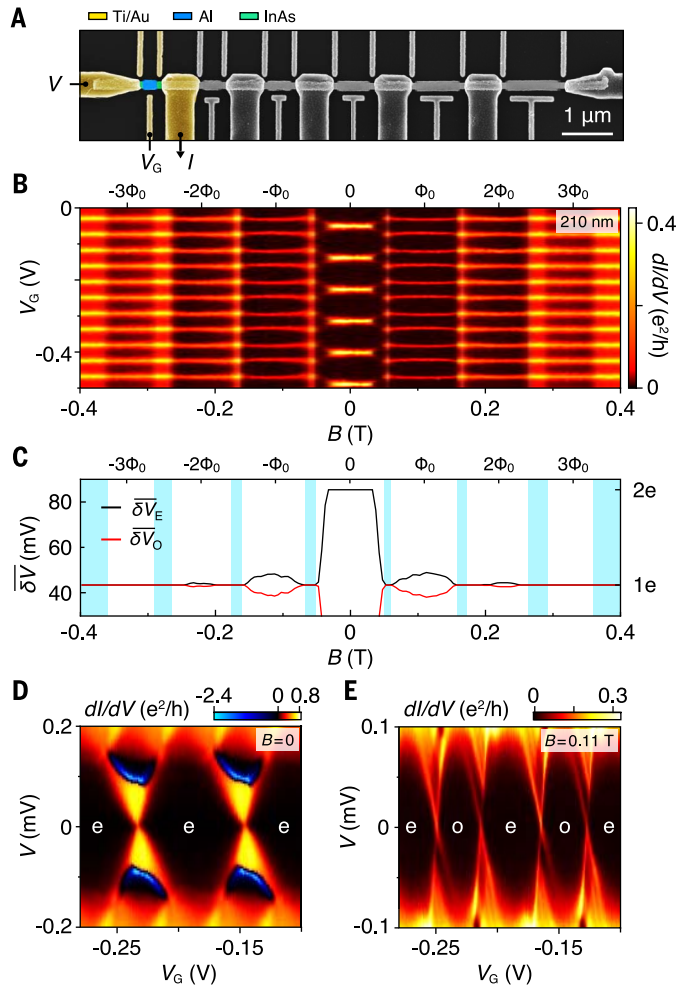
**Fig. 6. Coulomb blockade:  $2e$  peaks in the zeroth lobe, even-odd peaks in the first lobe.**

(A) Micrograph of device 2 comprising six islands with individual gates and leads, spanning a range of lengths from 210 to 970 nm. The measurement setup for the 210-nm segment is highlighted in color.

(B) Zero-bias conductance for the 210-nm segment measured at 20 mK showing Coulomb blockade evolution as a function of plunger gate voltage,  $V_G$ , and axial magnetic field,  $B$ .

(C) Average peak spacings for even (black) and odd (red) Coulomb valleys,  $\delta\bar{V}$ , from the data in (B) as a function of  $B$ , with destructive regimes shown in blue. Coulomb peaks spaced by  $2e$  split in field and become  $1e$ -periodic around 55 mT. At higher field, odd Coulomb valleys shrink, reaching a minimum around 120 mT. In the second destructive regime, around

165 mT, peaks are  $1e$ -periodic again. (D) Zero-field conductance as a function of  $V$  and  $V_G$ , showing  $2e$  Coulomb diamonds with even (e) valleys only. The negative differential conductance is associated with quasiparticle trapping on the island (see main text). (E) Similar to (D), but measured in the first lobe at  $B = 110$  mT; the data reveal discrete, near-zero-energy state, even (e) and odd (o) valleys of different sizes, and alternating excited state structure.



with an axial growth of InAs along the [0001] direction with wurtzite crystal structure, using an In flux corresponding to a planar InAs growth rate of 0.5  $\mu\text{m}/\text{hour}$  and a calibrated  $\text{As}_4/\text{In}$  flux ratio of 14. The InAs nanowires with core diameter of  $\sim 130$  nm were grown to a length of  $\sim 10$   $\mu\text{m}$ . Subsequently, an Al shell with thickness of  $\sim 30$  nm (or  $\sim 10$  nm for the nanowire used in device 4) was grown at  $-30^\circ\text{C}$  on all six facets by continuously rotating the growth substrate with respect to the metal source. The resulting full shell had an epitaxial, oxide-free interface between the Al and InAs (38).

The devices were fabricated on a degenerately n-doped Si substrate capped with a 200 nm thermal oxide. Before the wire deposition, the fabrication substrate was prefabricated with a set of alignment marks as well as bonding pads. Individual hybrid nanowires were transferred from the growth substrate

onto the fabrication substrate using a manipulator station with a tungsten needle. Standard electron beam lithography techniques were used to pattern etching windows, contacts, and gates.

The quality of the Al etching was found to improve when using a thin layer of AR 300-80 (new) adhesion promoter. Double layer of EL6 copolymer resists was used to define the etching windows. The Al was then selectively removed by submerging the fabrication substrate for  $\sim 70$  s into MF-321 photoresist developer.

As the native InAs and Al oxides have different work functions, different cleaning processes had to be applied before contacting the wires. To contact the Al shell in devices 1, 3, 4, and 5, a stack of A4 and A6 PMMA resists was used. Normal Ti/Al (5/210 nm) ohmic contacts to Al shell were deposited after in-situ Ar-ion milling (RF ion source, 25 W, 18 mTorr, 9 min). To contact the InAs core in all seven devices, a

single layer of A6 PMMA resist was used. A gentler Ar-ion milling (RF ion source, 15 W, 18 mTorr, 6.5 min) was used to clean the InAs core followed by metallization of the normal Ti/Al (5/180 nm) ohmic contacts to InAs core.

A single layer of A6 PMMA resist was used to form normal Ti/Al (5/150 nm) side-gate electrodes in devices 2, 6, and 7, and top-gate electrode in device 4, separated from the wire by  $\sim 8$  nm layer of atomic layer deposited dielectric  $\text{HfO}_2$ .

Each of the dc lines used to measure and gate the devices was equipped with RF and RC filters [QDevil (72)], giving an overall line resistance  $R_{\text{Line}} = 6.7$  kilohms per line. This has a negligible effect in a weak tunneling regime, where the device resistance is much greater than  $R_{\text{Line}}$ . In the strong tunneling regime, a substantial fraction of the applied voltage drops in the line resistance (dominated by the filters), resulting in smaller measured conductance. A comparison between measured two-terminal and numerically corrected spectra (fig. S4) is presented in (39). The four-probe differential resistance measurements were carried out using an ac excitation of  $I_{\text{ac}} = 200$  nA. The two-probe tunneling conductance measurements were conducted using an ac excitation of  $V_{\text{ac}} = 5$   $\mu\text{V}$ .

The normal-state Hamiltonian used in the numerical simulations is given by

$$\begin{aligned}
 H_0 = & \left[ (\vec{p} + eA_\phi \hat{\phi})^T / (2m(\vec{r})) \right] (\vec{p} + eA_\phi \hat{\phi}) \\
 & - E_F(\vec{r}) + U(\vec{r}) \sigma_0 \\
 & + \frac{1}{2} \left[ \alpha(\vec{r}) \hat{r} (\vec{\sigma} \times (\vec{p} + eA_\phi \hat{\phi})) \right. \\
 & \left. + \hat{r} (\vec{\sigma} \times (\vec{p} + eA_\phi \hat{\phi})) \alpha(\vec{r}) \right] \\
 & + Bg(\vec{r}) \frac{\mu_B}{2} \sigma_z
 \end{aligned} \quad (13)$$

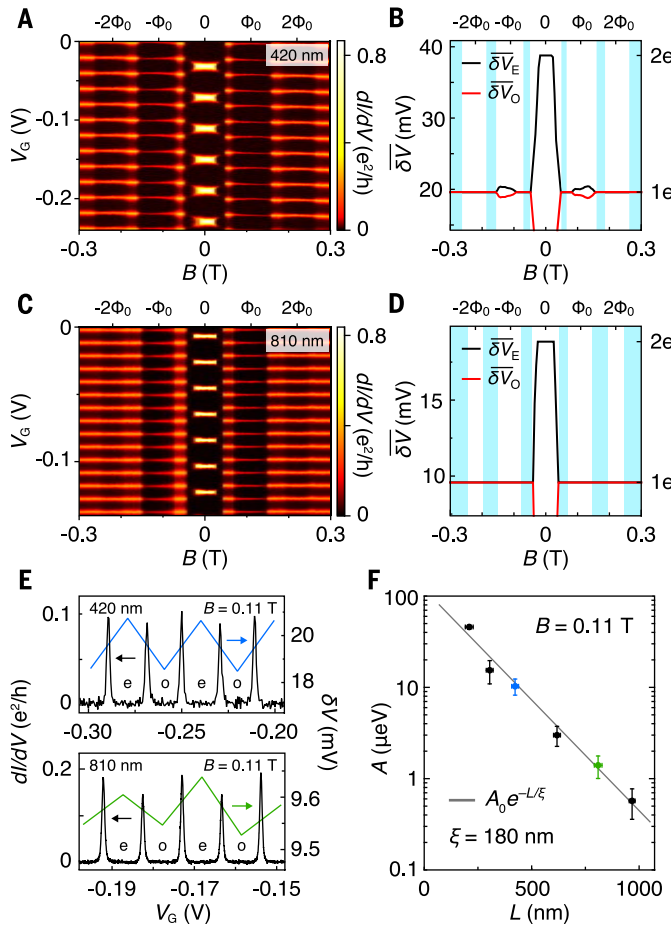
where  $E_F$  is the Fermi level,  $U$  is the potential energy, and  $\alpha$  is the radial spin-orbit coupling. We solve for the electrostatic potential in a separate step using the Thomas-Fermi approximation analog to (47). In the semiconductor (InAs), we take  $m_{\text{semi}} = 0.026m_e$ ,  $E_{F,\text{semi}} = 0$ , and  $g_{\text{semi}} = 14.7$  (73). In the superconductor (Al), we take  $m_{\text{super}} = m_e$ ,  $E_{F,\text{super}} = 11.7\text{eV}$ , and  $\alpha_{\text{super}} = g_{\text{super}} = 0$  (74). For simplicity we set  $g_{\text{super}} = 0$ . The vector potential  $A_\phi = Br/2$  corresponds to a spatially homogeneous magnetic field.

The Bogoliubov-de Gennes Hamiltonian is given by

$$\begin{aligned}
 H_{\text{BdG}} = & \\
 & \begin{bmatrix} H_0(\vec{r}, \vec{A}) - i\eta\sigma_0 & \Delta(\vec{r}) \\ \Delta^*(\vec{r}) & -\sigma_y H_0(\vec{r}, -\vec{A})^* \sigma_y - i\eta\sigma_0 \end{bmatrix}
 \end{aligned} \quad (14)$$

**Fig. 7. Length dependence of even-odd peak spacing.**

(A) Zero-bias conductance measured at 20 mK showing Coulomb blockade evolution with  $V_G$  and  $B$  for the 420-nm island. (B) Average peak spacing for data in (A). Even-odd pattern is evident in the first lobe, around  $B = 110$  mT. (C and D) Similar to (A) and (B), but for the 810-nm island. Even-odd spacing in the first lobe is not visible on this scale. (E) Fine-scale Coulomb peak conductance (black, left axis) and spacing (colored, right axis) as a function of plunger gate voltage,  $V_G$ , at  $B = 110$  mT for 420-nm and 810-nm islands. (F) Average even-odd peak spacing difference converted to energy,  $A$ , using separately measured level arms for each segment, at  $B = 110$  mT as a function of island length,  $L$ , along with the best fit to the exponential form  $A = A_0 e^{-L/\xi}$ , giving the best-fit parameters  $A_0 = 105 \mu\text{eV}$  and  $\xi = 180$  nm. Vertical error bars indicate uncertainties from standard deviation of  $\bar{\Delta V}$  and lever arms. Experimental noise floor,  $\sigma_A < 0.1 \mu\text{eV} \ll k_B T$ , measured using  $1e$  spacing in destructive regime. Horizontal error bars indicate uncertainties in lengths estimated from the micrograph.



where we introduce a small dissipative term  $\eta$ . It is numerically advantageous to introduce a small level broadening  $\eta = 2 \mu\text{eV}$  in the transport simulations to avoid sharp features. In all other simulations, we set  $\eta = 0$ . A side-effect of nonzero  $\eta$  is that the conductance becomes particle-hole-asymmetric for bias voltages below the Al gap (75). Nonzero  $\eta$  can also correspond to a soft-gap in the superconductor or result from coupling to an additional lead.

The superconductor is integrated-out into a self-energy boundary condition (39). The effective mass in Al is taken to be infinite parallel to the interface, and finite perpendicular to the interface (76). This means that in the discretized Hamiltonian, every lattice site adjacent to the superconductor is attached to a semi-infinite, one-dimensional Al chain. The idea behind this arrangement is to effectively simulate the fact that in the strong coupling limit there is nearly perfect Andreev reflection from the superconductor (77), as discussed in (39). In the semiconductor, we

use a lattice spacing of 5 nm. Because of the small  $\lambda_F$ , substantially smaller lattice spacing of 0.1 nm is required in Al. The non-equidistant discretization across the interface is described by the method of (34). For the InAs-Al bonds, we choose a length of 0.1 nm—the same as the discretization in Al—to ensure strong coupling.

We assume the following gap dependence within a lobe [see also eq. S11 in (39)]

$$\Delta_0(B, n) = \Delta_0(0, 0) \max\left(0, 1 - (nB_0/B_{\max})^2\right) \times \max\left(0, 1 - \xi_d^2/R^2(B/B_0 - n)^2\right) \quad (15)$$

with an effective radius  $R = 80$  nm and  $B_0 = \phi_0/(R^2 3\sqrt{3}/2)$  for a hexagonal cross section (78). The full pairing  $\Delta$  is then  $\Delta(\vec{r}, B, n = \lfloor \frac{B}{B_0} + 0.5 \rfloor) = \Delta_0(B, n)\Theta(\vec{r} \text{ in Al})e^{in\phi}$ . We take  $\Delta(0,0) = 0.24$  meV,  $\xi_d = 210$  nm and  $B_{\max} = 0.8$  T which results in a similar gap-field dependence as in the experiment (79).

## REFERENCES AND NOTES

- N. Read, D. Green, Paired states of fermions in two dimensions with breaking of parity and time-reversal symmetries and the fractional quantum Hall effect. *Phys. Rev. B* **61**, 10267–10297 (2000). doi: [10.1103/PhysRevB.61.10267](https://doi.org/10.1103/PhysRevB.61.10267)
- A. Y. Kitaev, Unpaired Majorana fermions in quantum wires. *Phys. Uspekhi* **44** (suppl.), 131–136 (2001). doi: [10.1070/1063-7869/44/10S/S29](https://doi.org/10.1070/1063-7869/44/10S/S29)
- J. Alicea, Y. Oreg, G. Refael, F. von Oppen, M. P. A. Fisher, Non-Abelian statistics and topological quantum information processing in 1D wire networks. *Nat. Phys.* **7**, 412–417 (2011). doi: [10.1038/nphys1915](https://doi.org/10.1038/nphys1915)
- C. Nayak, S. H. Simon, A. Stern, M. Freedman, S. Das Sarma, Non-Abelian anyons and topological quantum computation. *Rev. Mod. Phys.* **80**, 1083–1159 (2008). doi: [10.1103/RevModPhys.80.1083](https://doi.org/10.1103/RevModPhys.80.1083)
- S. D. Sarma, M. Freedman, C. Nayak, Majorana zero modes and topological quantum computation. *NPJ Quant. Inf.* **1**, 15001 (2015). doi: [10.1038/npjqi.2015.1](https://doi.org/10.1038/npjqi.2015.1)
- R. M. Lutchyn, J. D. Sau, S. Das Sarma, Majorana fermions and a topological phase transition in semiconductor-superconductor heterostructures. *Phys. Rev. Lett.* **105**, 077001 (2010). doi: [10.1103/PhysRevLett.105.077001](https://doi.org/10.1103/PhysRevLett.105.077001); pmid: [20868069](https://pubmed.ncbi.nlm.nih.gov/20868069/)
- Y. Oreg, G. Refael, F. von Oppen, Helical liquids and Majorana bound states in quantum wires. *Phys. Rev. Lett.* **105**, 177002 (2010). doi: [10.1103/PhysRevLett.105.177002](https://doi.org/10.1103/PhysRevLett.105.177002); pmid: [21231073](https://pubmed.ncbi.nlm.nih.gov/21231073/)
- V. Mourik *et al.*, Signatures of Majorana fermions in hybrid superconductor-semiconductor nanowire devices. *Science* **336**, 1003–1007 (2012). doi: [10.1126/science.1222360](https://doi.org/10.1126/science.1222360); pmid: [2249805](https://pubmed.ncbi.nlm.nih.gov/2249805/)
- M. T. Deng *et al.*, Majorana bound state in a coupled quantum-dot hybrid-nanowire system. *Science* **354**, 1557–1562 (2016). doi: [10.1126/science.aaf39861](https://doi.org/10.1126/science.aaf39861); pmid: [28008065](https://pubmed.ncbi.nlm.nih.gov/28008065/)
- S. M. Albrecht *et al.*, Exponential protection of zero modes in Majorana islands. *Nature* **531**, 206–209 (2016). doi: [10.1038/nature17162](https://doi.org/10.1038/nature17162); pmid: [26961654](https://pubmed.ncbi.nlm.nih.gov/26961654/)
- H. Zhang *et al.*, Quantized Majorana conductance. *Nature* **556**, 74–79 (2018). doi: [10.1038/nature26142](https://doi.org/10.1038/nature26142); pmid: [29590094](https://pubmed.ncbi.nlm.nih.gov/29590094/)
- R. M. Lutchyn *et al.*, Majorana zero modes in superconductor-semiconductor heterostructures. *Nat. Rev. Mater.* **3**, 52–68 (2018). doi: [10.1038/s41578-018-0003-1](https://doi.org/10.1038/s41578-018-0003-1)
- L. Fu, C. L. Kane, Superconducting proximity effect and majorana fermions at the surface of a topological insulator. *Phys. Rev. Lett.* **100**, 096407 (2008). doi: [10.1103/PhysRevLett.100.096407](https://doi.org/10.1103/PhysRevLett.100.096407); pmid: [18352737](https://pubmed.ncbi.nlm.nih.gov/18352737/)
- C.-K. Chiu, M. J. Gilbert, T. L. Hughes, Vortex lines in topological insulator-superconductor heterostructures. *Phys. Rev. B* **84**, 144507 (2011). doi: [10.1103/PhysRevB.84.144507](https://doi.org/10.1103/PhysRevB.84.144507)
- A. Cook, M. Franz, Majorana fermions in a topological-insulator nanowire proximity-coupled to an s-wave superconductor. *Phys. Rev. B* **84**, 201105 (2011). doi: [10.1103/PhysRevB.84.201105](https://doi.org/10.1103/PhysRevB.84.201105)
- F. de Juan, R. Ilan, J. H. Bardarson, Robust transport signatures of topological superconductivity in topological insulator nanowires. *Phys. Rev. Lett.* **113**, 107003 (2014). doi: [10.1103/PhysRevLett.113.107003](https://doi.org/10.1103/PhysRevLett.113.107003); pmid: [25238379](https://pubmed.ncbi.nlm.nih.gov/25238379/)
- J.-P. Xu *et al.*, Experimental detection of a Majorana mode in the core of a magnetic vortex inside a topological insulator-superconductor  $\text{Bi}_2\text{Te}_3/\text{NbSe}_2$  heterostructure. *Phys. Rev. Lett.* **114**, 017001 (2015). doi: [10.1103/PhysRevLett.114.017001](https://doi.org/10.1103/PhysRevLett.114.017001); pmid: [25615497](https://pubmed.ncbi.nlm.nih.gov/25615497/)
- J. D. Sau, R. M. Lutchyn, S. Tewari, S. Das Sarma, Generic new platform for topological quantum computation using semiconductor heterostructures. *Phys. Rev. Lett.* **104**, 040502 (2010). doi: [10.1103/PhysRevLett.104.040502](https://doi.org/10.1103/PhysRevLett.104.040502); pmid: [20366693](https://pubmed.ncbi.nlm.nih.gov/20366693/)
- J. Alicea, Majorana fermions in a tunable semiconductor device. *Phys. Rev. B* **81**, 125318 (2010). doi: [10.1103/PhysRevB.81.125318](https://doi.org/10.1103/PhysRevB.81.125318)
- P. Hosur, P. Ghaemi, R. S. K. Mong, A. Vishwanath, Majorana modes at the ends of superconductor vortices in doped topological insulators. *Phys. Rev. Lett.* **107**, 097001 (2011). doi: [10.1103/PhysRevLett.107.097001](https://doi.org/10.1103/PhysRevLett.107.097001); pmid: [21929261](https://pubmed.ncbi.nlm.nih.gov/21929261/)
- D. Wang *et al.*, Evidence for Majorana bound states in an iron-based superconductor. *Science* **362**, 333–335 (2018). doi: [10.1126/science.aao1797](https://doi.org/10.1126/science.aao1797); pmid: [30115743](https://pubmed.ncbi.nlm.nih.gov/30115743/)
- S. Das Sarma, M. Freedman, C. Nayak, Topologically protected qubits from a possible non-Abelian fractional quantum Hall state. *Phys. Rev. Lett.* **94**, 166802 (2005). doi: [10.1103/PhysRevLett.94.166802](https://doi.org/10.1103/PhysRevLett.94.166802); pmid: [15904258](https://pubmed.ncbi.nlm.nih.gov/15904258/)
- A. Romito, J. Alicea, G. Refael, F. von Oppen, Manipulating Majorana fermions using supercurrents. *Phys. Rev. B* **85**, 020502 (2012). doi: [10.1103/PhysRevB.85.020502](https://doi.org/10.1103/PhysRevB.85.020502)

24. B. van Heck, S. Mi, A. R. Akhmerov, Single fermion manipulation via superconducting phase differences in multiterminal Josephson junctions. *Phys. Rev. B* **90**, 155450 (2014). doi: [10.1103/PhysRevB.90.155450](https://doi.org/10.1103/PhysRevB.90.155450)
25. P. Kotetes, Topological superconductivity in Rashba semiconductors without a Zeeman field. *Phys. Rev. B* **92**, 014514 (2015). doi: [10.1103/PhysRevB.92.014514](https://doi.org/10.1103/PhysRevB.92.014514)
26. M. Hell, M. Leijnse, K. Flensberg, Two-dimensional platform for networks of Majorana bound states. *Phys. Rev. Lett.* **118**, 107701 (2017). doi: [10.1103/PhysRevLett.118.107701](https://doi.org/10.1103/PhysRevLett.118.107701); pmid: 28339276
27. F. Pientka *et al.*, Topological superconductivity in a planar Josephson junction. *Phys. Rev. X* **7**, 021032 (2017). doi: [10.1103/PhysRevX.7.021032](https://doi.org/10.1103/PhysRevX.7.021032)
28. T. D. Stanescu, A. Sitek, A. Manolescu, Robust topological phase in proximitized core-shell nanowires coupled to multiple superconductors. *Beilstein J. Nanotechnol.* **9**, 1512–1526 (2018). doi: [10.3762/bjnano.9.142](https://doi.org/10.3762/bjnano.9.142); pmid: 29977684
29. W. A. Little, R. D. Parks, Observation of quantum periodicity in the transition temperature of a superconducting cylinder. *Phys. Rev. Lett.* **9**, 9–12 (1962). doi: [10.1103/PhysRevLett.9.9](https://doi.org/10.1103/PhysRevLett.9.9)
30. P.-G. de Gennes, *Physique des Basses Températures*. C. R. Acad. Sci. Paris **292**, 279 (1981).
31. Y. Liu *et al.*, Destruction of the global phase coherence in ultrathin, doubly connected superconducting cylinders. *Science* **294**, 2332–2334 (2001). doi: [10.1126/science.1066144](https://doi.org/10.1126/science.1066144); pmid: 11743195
32. I. Sternfeld *et al.*, Magnetoresistance oscillations of superconducting Al-film cylinders covering InAs nanowires below the quantum critical point. *Phys. Rev. Lett.* **107**, 037001 (2011). doi: [10.1103/PhysRevLett.107.037001](https://doi.org/10.1103/PhysRevLett.107.037001); pmid: 21838393
33. M. Tinkham, *Introduction to Superconductivity* (McGraw Hill, ed. 2, 1996).
34. A. E. Antipov *et al.*, Effects of gate-induced electric fields on semiconductor Majorana nanowires. *Phys. Rev. X* **8**, 031041 (2018). doi: [10.1103/PhysRevX.8.031041](https://doi.org/10.1103/PhysRevX.8.031041)
35. A. E. G. Mikkelsen, P. Kotetes, P. Krogstrup, K. Flensberg, Hybridization at superconductor-semiconductor interfaces. *Phys. Rev. X* **8**, 031040 (2018). doi: [10.1103/PhysRevX.8.031040](https://doi.org/10.1103/PhysRevX.8.031040)
36. B. D. Woods, S. Das Sarma, T. D. Stanescu, Electronic structure of full-shell InAs/Al hybrid semiconductor-superconductor nanowires: Spin-orbit coupling and topological phase space. *Phys. Rev. B* **99**, 161118 (2019). doi: [10.1103/PhysRevB.99.161118](https://doi.org/10.1103/PhysRevB.99.161118)
37. B. van Heck, R. M. Lutchyn, L. I. Glazman, Conductance of a proximitized nanowire in the Coulomb blockade regime. *Phys. Rev. B* **93**, 235431 (2016). doi: [10.1103/PhysRevB.93.235431](https://doi.org/10.1103/PhysRevB.93.235431)
38. P. Krogstrup *et al.*, Epitaxy of semiconductor-superconductor nanowires. *Nat. Mater.* **14**, 400–406 (2015). doi: [10.1038/nmat4176](https://doi.org/10.1038/nmat4176); pmid: 25581626
39. See supplementary materials.
40. J. M. Gordon, C. J. Lobb, M. Tinkham, Divergent phase-breaking rate in aluminum films from magnetoconductance measurements. *Phys. Rev. B* **29**, 5232–5235 (1984). doi: [10.1103/PhysRevB.29.5232](https://doi.org/10.1103/PhysRevB.29.5232)
41. C. Kittel, *Introduction to Solid State Physics* (Wiley, ed. 8, 2005).
42. G. Schwiete, Y. Oreg, Persistent current in small superconducting rings. *Phys. Rev. Lett.* **103**, 037001 (2009). doi: [10.1103/PhysRevLett.103.037001](https://doi.org/10.1103/PhysRevLett.103.037001); pmid: 19659307
43. C. Caroli, P. G. De Gennes, J. Matricon, Bound Fermion states on a vortex line in a type II superconductor. *Phys. Lett.* **9**, 307–309 (1964). doi: [10.1016/0031-9163\(64\)90375-0](https://doi.org/10.1016/0031-9163(64)90375-0)
44. A. Vuik, B. Nijholt, A. R. Akhmerov, M. Wimmer, Reproducing topological properties with quasi-Majorana states. *SciPost Phys.* **7**, 061 (2019). doi: [10.21468/SciPostPhys.7.5.061](https://doi.org/10.21468/SciPostPhys.7.5.061)
45. Note that magnetic flux piercing the finite-thickness superconducting shell can be substantially different from that penetrating the core.
46. A. Vuik, D. Eeltink, A. R. Akhmerov, M. Wimmer, Effects of the electrostatic environment on the Majorana nanowire devices. *New J. Phys.* **18**, 033013 (2016). doi: [10.1088/1367-2630/18/3/033013](https://doi.org/10.1088/1367-2630/18/3/033013)
47. G. W. Winkler *et al.*, Unified numerical approach to topological semiconductor-superconductor heterostructures. *Phys. Rev. B* **99**, 245408 (2019). doi: [10.1103/PhysRevB.99.245408](https://doi.org/10.1103/PhysRevB.99.245408)
48. G. W. Winkler *et al.*, Orbital contributions to the electron g factor in semiconductor nanowires. *Phys. Rev. Lett.* **119**, 037701 (2017). doi: [10.1103/PhysRevLett.119.037701](https://doi.org/10.1103/PhysRevLett.119.037701); pmid: 28777644
49. S. Schuwallow *et al.*, Band bending profile and band offset extraction at semiconductor-metal interfaces. *arXiv:1910.02735 [cond-mat.mtrl-sci]* (7 October 2019).
50. With our sign convention, this electric field results in an  $\alpha$  of negative sign. However, there are also other contributions to  $\alpha$  from strain and microscopic details of the InAs-Al interface. Therefore, the sign of the spin-orbit coupling is difficult to predict.
51. R. Winkler, *Spin-Orbit Coupling Effects in Two-Dimensional Electron and Hole Systems* (Springer Tracts in Modern Physics, Springer, 2003).
52. M. Wimmer, Algorithm 923. *ACM Trans. Math. Softw.* **38**, 30 (2012). doi: [10.1145/2331130.2331138](https://doi.org/10.1145/2331130.2331138)
53. D. Sticlet, B. Nijholt, A. Akhmerov, Robustness of Majorana bound states in the short-junction limit. *Phys. Rev. B* **95**, 115421 (2017). doi: [10.1103/PhysRevB.95.115421](https://doi.org/10.1103/PhysRevB.95.115421)
54. R. M. Lutchyn, M. P. A. Fisher, Interacting topological phases in multiband nanowires. *Phys. Rev. B* **84**, 214528 (2011). doi: [10.1103/PhysRevB.84.214528](https://doi.org/10.1103/PhysRevB.84.214528)
55. B. Nijholt, A. R. Akhmerov, Orbital effect of magnetic field on the Majorana phase diagram. *Phys. Rev. B* **93**, 235434 (2016). doi: [10.1103/PhysRevB.93.235434](https://doi.org/10.1103/PhysRevB.93.235434)
56. C. W. Groth, M. Wimmer, A. R. Akhmerov, X. Waintal, Kwant: A software package for quantum transport. *New J. Phys.* **16**, 063065 (2014). doi: [10.1088/1367-2630/16/6/063065](https://doi.org/10.1088/1367-2630/16/6/063065)
57. B. Nijholt, J. Weston, J. Hoofwijk, A. Akhmerov, *Adaptive: parallel active learning of mathematical functions* (2019); <https://github.com/python-adaptive/adaptive>.
58. The asymmetry of the conductance of subgap states in bias voltage in our simulation is a consequence of a dissipation term  $\eta = 2 \mu\text{eV}$  (72).
59. E. C. T. O'Farrell *et al.*, Hybridization of subgap states in one-dimensional superconductor-semiconductor Coulomb islands. *Phys. Rev. Lett.* **121**, 256803 (2018). doi: [10.1103/PhysRevLett.121.256803](https://doi.org/10.1103/PhysRevLett.121.256803); pmid: 30608825
60. J. Shen *et al.*, Parity transitions in the superconducting ground state of hybrid InSb-Al Coulomb islands. *Nat. Commun.* **9**, 4801 (2018). doi: [10.1038/s41467-018-07279-7](https://doi.org/10.1038/s41467-018-07279-7); pmid: 30442935
61. M. Cheng, R. M. Lutchyn, V. Galitski, S. Das Sarma, Splitting of Majorana-fermion modes due to intervertex tunneling in a  $p_x + i p_y$  superconductor. *Phys. Rev. Lett.* **103**, 107001 (2009). doi: [10.1103/PhysRevLett.103.107001](https://doi.org/10.1103/PhysRevLett.103.107001); pmid: 19792335
62. L. Fu, Electron teleportation via Majorana bound states in a mesoscopic superconductor. *Phys. Rev. Lett.* **104**, 056402 (2010). doi: [10.1103/PhysRevLett.104.056402](https://doi.org/10.1103/PhysRevLett.104.056402); pmid: 20366777
63. C.-K. Chiu, J. D. Sau, S. Das Sarma, Conductance of a superconducting Coulomb-blockaded Majorana nanowire. *Phys. Rev. B* **96**, 054504 (2017). doi: [10.1103/PhysRevB.96.054504](https://doi.org/10.1103/PhysRevB.96.054504)
64. F. W. J. Hekking, L. I. Glazman, K. A. Matveev, R. I. Shekhter, Coulomb blockade of two-electron tunneling. *Phys. Rev. Lett.* **70**, 4138–4141 (1993). doi: [10.1103/PhysRevLett.70.4138](https://doi.org/10.1103/PhysRevLett.70.4138); pmid: 10054056
65. J. M. Hergenrother, M. T. Tuominen, M. Tinkham, Charge transport by Andreev reflection through a mesoscopic superconducting island. *Phys. Rev. Lett.* **72**, 1742–1745 (1994). doi: [10.1103/PhysRevLett.72.1742](https://doi.org/10.1103/PhysRevLett.72.1742); pmid: 10055689
66. A. P. Higginbotham *et al.*, Parity lifetime of bound states in a proximitized semiconductor nanowire. *Nat. Phys.* **11**, 1017–1021 (2015). doi: [10.1038/nphys3461](https://doi.org/10.1038/nphys3461)
67. J. M. Thijsen, H. S. J. Van der Zant, Charge transport and single-electron effects in nanoscale systems. *Phys. Stat. Sol. B* **245**, 1455–1470 (2008). doi: [10.1002/pssb.200743470](https://doi.org/10.1002/pssb.200743470)
68. E. B. Hansen, J. Danon, K. Flensberg, Probing electron-hole components of subgap states in Coulomb-blockaded Majorana islands. *Phys. Rev. B* **97**, 041411 (2018). doi: [10.1103/PhysRevB.97.041411](https://doi.org/10.1103/PhysRevB.97.041411)
69. T. D. Stanescu, R. M. Lutchyn, S. Das Sarma, Majorana fermions in semiconductor nanowires. *Phys. Rev. B* **84**, 144522 (2011). doi: [10.1103/PhysRevB.84.144522](https://doi.org/10.1103/PhysRevB.84.144522)
70. S. Nadj-Perge, I. K. Drozdov, B. A. Bernevig, A. Yazdani, Proposal for realizing Majorana fermions in chains of magnetic atoms on a superconductor. *Phys. Rev. B* **88**, 020407 (2013). doi: [10.1103/PhysRevB.88.020407](https://doi.org/10.1103/PhysRevB.88.020407)
71. Y. Peng, F. Pientka, L. I. Glazman, F. von Oppen, Strong localization of Majorana end States in chains of magnetic adatoms. *Phys. Rev. Lett.* **114**, 106801 (2015). doi: [10.1103/PhysRevLett.114.106801](https://doi.org/10.1103/PhysRevLett.114.106801); pmid: 25815952
72. QDevil ApS; [www.qdevil.com](http://www.qdevil.com).
73. I. Vurgaftman, J. R. Meyer, L. R. Ram-Mohan, Band parameters for III-V compound semiconductors and their alloys. *J. Appl. Phys.* **89**, 5815–5875 (2001). doi: [10.1063/1.1368156](https://doi.org/10.1063/1.1368156)
74. N. Ashcroft, N. Mermin, *Solid State Physics* (Cengage Learning, 2011).
75. C.-X. Liu, J. D. Sau, T. D. Stanescu, S. Das Sarma, Andreev bound states versus Majorana bound states in quantum dot-nanowire-superconductor hybrid structures: Trivial versus topological zero-bias conductance peaks. *Phys. Rev. B* **96**, 075161 (2017). doi: [10.1103/PhysRevB.96.075161](https://doi.org/10.1103/PhysRevB.96.075161)
76. This approximation is well justified given the much larger effective mass of Al compared with InAs (80).
77. T. Kiendl, F. von Oppen, P. W. Brouwer, Proximity-induced gap in nanowires with a thin superconducting shell. *Phys. Rev. B* **100**, 035426 (2019). doi: [10.1103/PhysRevB.100.035426](https://doi.org/10.1103/PhysRevB.100.035426)
78.  $R$  is measured from the center to a corner of an effective hexagon.
79. Although the  $\xi_d$  chosen in the simulation is slightly different from the experimentally measured  $\xi_S = 180$  nm, the gap-field dependence is still very close in simulation and experiment.
80. T. O. Rosdahl, A. Vuik, M. Kjaergaard, A. R. Akhmerov, Andreev rectifier: A nonlocal conductance signature of topological phase transitions. *Phys. Rev. B* **97**, 045421 (2018). doi: [10.1103/PhysRevB.97.045421](https://doi.org/10.1103/PhysRevB.97.045421)
81. S. Vaitiekėnas *et al.*, Replication data for: Flux-induced topological superconductivity in full-shell nanowires, Version 1, Zenodo (2020); <https://doi.org/10.5281/zenodo.3585690>.
82. S. Vaitiekėnas *et al.*, Simulation code for: Flux-induced topological superconductivity in full-shell nanowires, Version 1, Zenodo (2020); <https://doi.org/10.5281/zenodo.3636085>.

## ACKNOWLEDGMENTS

We thank A. Antipov, L. Casparis, M. Freedman, A. Higginbotham, and E. Martinez for valuable discussions; J. Gamble and J. Gukelberger for contributions to the simulation code; and C. Sørensen, R. Tanta, and S. Upadhyay for contributions to material growth and device fabrication. **Funding:** Research was supported by Microsoft, the Danish National Research Foundation, and the European Commission. This work was performed in part at the Aspen Center for Physics, which is supported by National Science Foundation (NSF) grant PHY-1607611. M.-T.D. acknowledges support from State Key Laboratory of High Performance Computing, China. L.I.G. acknowledges support from NSF Division of Materials Research grant 1603243. **Author contributions:** P.K. developed the nanowire materials. S.V. fabricated the devices, performed measurements, and analyzed the data with input from M.-T.D. and C.M.M. The analytical model was developed by R.M.L., B.v.H., and T.K. with input from G.W.W., K.F., L.I.G., and C.N. Numerical simulations were performed by G.W.W. and B.v.H. with input from R.M.L., T.K., and L.I.G. All authors contributed to writing the manuscript. Correspondence pertaining to theory should be directed to R.M.L., and correspondence pertaining to experiment should be directed to C.M.M. **Competing interests:** A patent application (US20200027030/971 A1) related to full-shell nanowires with application to quantum computing was filed by B.v.H., G.W.W., T.K., R.M.L., P.K., C.N., C.M.M., S.V., and others. **Data and materials availability:** Data for figures (81) and simulation code (82) are available online.

## SUPPLEMENTARY MATERIALS

[science.sciencemag.org/content/367/6485/eaav3392/suppl/DC1](https://science.sciencemag.org/content/367/6485/eaav3392/suppl/DC1)  
Supplementary Text  
Figs. S1 to S24  
Table S1  
References (83–89)

6 September 2018; resubmitted 4 August 2019  
Accepted 27 February 2020  
[10.1126/science.aav3392](https://doi.org/10.1126/science.aav3392)

## Flux-induced topological superconductivity in full-shell nanowires

S. Vaitiek#nasG. W. WinklerB. van HeckT. KarzigM.-T. DengK. FlensbergL. I. GlazmanC. NayakP. KrogstrupR. M. LutchynC. M. Marcus

*Science*, 367 (6485), eaav3392.

### A possible Majorana sighting

Majorana zero modes, exotic quasiparticles predicted to occur in topological superconductors, hold promise as a building block of topological quantum computing. Two of the frontrunners for the physical implementation of Majoranas include hybrid semiconductor-superconductor nanowires and topological insulators in contact with a superconductor. Vaitiek#nas *et al.* introduce a platform that combines elements of both: a semiconductor nanowire that is fully wrapped by a superconductor. Combining theoretical calculations with experiments, the researchers present evidence that is consistent with the emergence of Majorana zero modes in this system.

*Science*, this issue p. eaav3392

### View the article online

<https://www.science.org/doi/10.1126/science.aav3392>

### Permissions

<https://www.science.org/help/reprints-and-permissions>

Use of think article is subject to the [Terms of service](#)

---

*Science* (ISSN 1095-9203) is published by the American Association for the Advancement of Science. 1200 New York Avenue NW, Washington, DC 20005. The title *Science* is a registered trademark of AAAS.

Copyright © 2020 The Authors, some rights reserved; exclusive licensee American Association for the Advancement of Science. No claim to original U.S. Government Works

# Post-publication analysis of ‘Flux-tuned topological superconductivity in full-shell nanowires’ Vaitiekėnas et al. Science 2020

Sergey Frolov, University of Pittsburgh  
Vincent Mourik, University of New South Wales

Sept 30 2021, Version 2

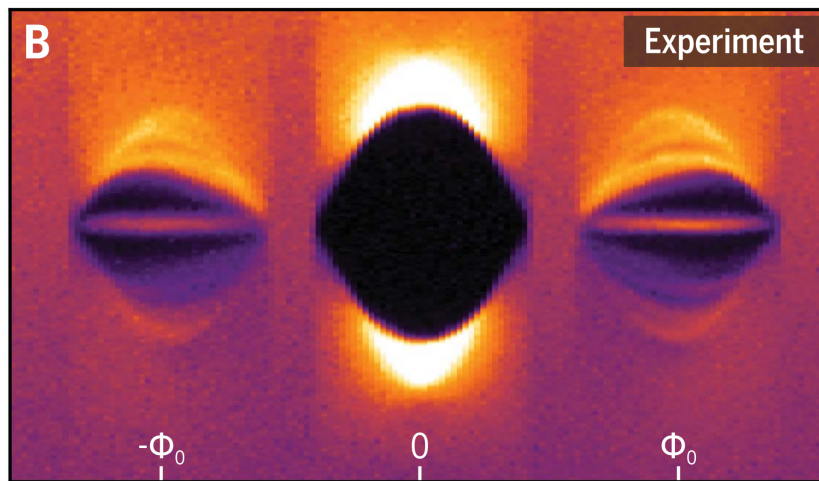
<b>1. Summary of our findings</b>	<b>2</b>
1.2 Who we are	3
1.3 What this analysis is based upon	3
<b>2. Background information on the physics of Majorana states</b>	<b>4</b>
2.2 Measurement techniques used	5
<b>3. Analysis of tunneling data (Figure 2)</b>	<b>6</b>
3.2 Gate-dependent zero-bias peaks	8
<b>4. Device-to-device reproducibility</b>	<b>13</b>
4.2 Even/odd pattern	14
4.3 Empty gap within LP-0 (near zero magnetic field)	15
4.4 More examples illustrate the large variety of observed phenomena	16
4.5 Device 5: “bad” device with no ZBP but with Andreev Bound States	18
<b>5. Discussion of the paper text and other figures</b>	<b>19</b>
5.2 Comments on the theory part	20
5.3 Comment on Coulomb blockade section	22
5.4 Comment on related results from Austria	23
5.5 Summary of communications with the authors of the paper	24
<b>APPENDIX A - Relevant quotations from the Science-2020 paper</b>	<b>25</b>
A.1 Statements about Majorana in the paper	25
A.2 On tunneling spectroscopy at zero magnetic field:	25
A.3 On tunneling spectroscopy within the first lobe of the Little-Parks oscillations	26
A.4 On tunneling spectroscopy within the second lobe of the Little-Parks oscillations:	27
A.5 On tunneling spectroscopy within the third lobe of the Little-Parks oscillations:	28
A.6 On device 5 where no ZBP was shown (some quotes already included earlier):	28

## 1. Summary of our findings

In March 2020 a paper was published in *Science* titled “Flux-induced topological superconductivity in full-shell nanowires”

<https://science.sciencemag.org/content/367/6485/eaav3392> (in what follows Science-2020)

Having carefully studied the paper, as well as additional data that were only made available after the paper was published, we conclude the following.



*Key data of the paper, showing a pattern that is irreproducible in the larger dataset. From the Research Article Summary of the Science-2020 paper.*

Data in the key Figure 2 are not representative of the full experimental data obtained. The additional data contain datasets that contradict Figure 2 in significant ways. Contradictions are found in data over larger parameter ranges from the same device, as well as in analogous data from other devices.

With respect to data as shown in Figure 2, multiple statements throughout the paper are irreproducible or misleading. These statements concern both the description of the data, as well as the interpretation of the data as relevant to ‘flux-induced topological superconductivity’ - the topic of the paper. Thus the core conclusions of the paper are invalidated. We do not see how this paper can remain in the present form, nor how the problem can be addressed by publishing any form of clarification such as a correction.

Selection of data for publication or for another form of presentation is an inevitable part of the research process. Hundreds or thousands of datasets are obtained for each study in our field. Yet only 5-10 become figures in a given paper. Here we identify a situation in which the selection of data for this paper is not representative of the total data obtained. This could be a consequence of one or several factors. We do not attempt to assign a particular explanation as to why data were chosen in a non-representative way.

In this update (V2) of the post-publication analysis we incorporate the statement by Niels Bohr Institute Director Jan Thomsen that data shared in November 2020 is all of the available data. If this statement is accepted, this provides a second reason to consider editorial retraction. The volume of data (52 datafiles relevant to Figure 2) is insufficient to make a scientific claim due to the large parameter spaces, device-to-device variations, variety of phenomena, and temporal instabilities that these nanowires display. The paper from IST Austria published in Science in 2021 that finds no Majorana in the same nanowires is supported by the body of data that is at least 10 times that declared by NBI Copenhagen. Additionally, if the statement of Thomsen is to be believed, then our initial analysis from June 1 2021 (v1 of this document) is based on the full body of data, which means that no further data that could overturn or clarify our conclusions will be forthcoming.

## 1.2 Who we are

Sergey Frolov (SF) is an associate professor at the University of Pittsburgh specializing in experimental condensed matter physics, in particular on transport experiments on low dimensional systems at cryogenic temperatures. Vincent Mourik (VM) is a postdoctoral scholar at UNSW focusing on spin physics in silicon defects. Majorana research has been the topic of the PhD work of VM. SF has been focusing on Majorana in his research for the past 10 years. Both VM and SF have written articles for *Science* and are familiar with editorial policies and standards. Neither SF nor VM are driven by personal or other disqualifying motives to misrepresent our findings in any way to the magazine.

## 1.3 What this analysis is based upon

Our analysis is based on publicly available materials and can be verified and reproduced by third parties. The available data that are relevant to Figure 2 of Science-2020 paper is 52 datasets from tunneling measurements. We perform our analysis under the assumption that these data are the best available in support of the claims of the paper. This is because the authors shared the additional data in response to a request from us that clearly stated our goal was to re-analyze their results.

Data can be found at: <http://doi.org/10.5281/zenodo.4263106> and can be split in three groups:

•**The *Science-2020* paper main figures:** In March 2020, *Science* published a paper 'Flux-induced topological superconductivity in full-shell nanowires'.

•**SOM:** Supplementary Online Materials published with the *Science-2020* paper.

•**Additional data:** On August 18 2020 we asked the corresponding authors of the *Science-2020* paper to share more data. They uploaded more data on November 8 2020. These data can be found in `additional_data.zip` on Zenodo.

Typically many more samples are studied that inform a given paper than those presented in the paper. The Zenodo repository gives the number of samples that exhibited ZBP as 9. All those studied samples and data obtained are part of the full volume of data. The conclusions of the paper are based upon those even if the data are not presented within the paper. Data obtained at a later moment in time, after the publication, or by different researchers, are not part of the full volume of data for the published study.

A dataset is a single graph, usually derived from executing a measurement script on a measurement computer that controls the measurement equipment. In the original form, a dataset is a spreadsheet of numbers that can be plotted as a curve or a two-dimensional colormap. ‘Original’ refers to the datafile, a settings file and a script as recorded at the moment of the measurement, without any further alteration. Sometimes ‘raw data’ is used which some people use to describe original data and others to describe any spreadsheet data including those already processed, e.g. for publication. To us, ‘raw data’, or ‘full data’ imply what we describe here as the original data.

## 2. Background information on the physics of Majorana states

It is not required to be an expert on Majorana research to understand our findings. In fact, little to none of the Majorana physics is involved in our arguments because the issue we identify is the lack of reproducibility of the regimes shown in the figures. However, it is helpful to know several well-established and non-controversial facts about Majorana states and their relationship to the specific subject of the *Science-2020* paper.

Names used for this phenomenon are: Majorana fermions, Majorana bound states (MBS), Majorana zero modes (MZM). A regime in which Majorana modes are present is commonly referred to as ‘topological regime’ or ‘topological superconductor’. The title of the *Science-2020* paper contains the words ‘topological superconductivity’, and the authors describe their observation of Majorana modes in the paper.

Majorana states have been predicted to produce conductance peaks in electronic transport measurements. These peaks are expected at zero source-drain bias voltage, hence Majorana Zero Modes. The peaks are referred to as zero-bias peaks (ZBP) or zero-bias conductance peaks (ZBCP). They are expected to not be transient, but rather

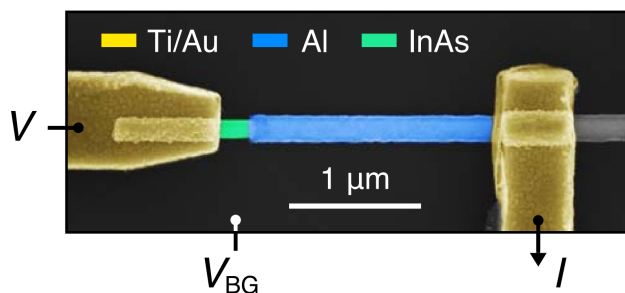
remain at zero voltage while electric and magnetic fields are varied by experimentalists over some range.

It is also important to know that Majorana is not the only phenomenon that results in non-transient zero bias peaks. Another well-studied effect is called Andreev bound states and such states are expected to form much more easily than Majorana states, meaning they can exist over much wider ranges of experimental parameters. It is known, at least since 2014, that under certain conditions Andreev bound states can generate non-transient ZBCPs that can mimic Majorana states. Andreev states are sometimes called 'trivial', which is understood as 'not a Majorana state' and/or 'not topological'.

Having provided this background, we emphasize that the conclusions of the present analysis and its findings do not depend on the currently ongoing scientific debates about whether evidence supporting the existence of Majorana modes in any device or materials platform has been already obtained. We do not rely on the present scientific understanding of this question, and we do not rely on any research that has taken place after 2018, the date of the initial posting of results on arXiv. Instead, our analysis is confined to checking for consistency between written statements and the figures presented by the authors in their Science-2020 paper, and the larger dataset now available.

## 2.2 Measurement techniques used

The technique used to obtain data in Figure 2 is electrical measurements where a small bias voltage is applied across a sample and current, or conductance (the change in current as bias voltage varies), is measured. This is the technique used to search for a ZBP in nanowire devices. Devices studied this way are referred to by the authors as 'NIS' (normal-insulator-superconductor). This is because a separate voltage on a nearby gate electrode is used to deplete a segment of the bare semiconductor nanowire in a field effect transistor-like manner. This creates an insulating segment located between superconductor and non-superconductor (normal) metal contacts. Electrons have to quantum-mechanically tunnel across the insulating segment, so a zero-bias peak is obtained in a tunneling or a tunneling spectroscopy measurement.



*A segment of Figure 2A. Source-drain voltage bias  $V$  is applied to normal contact (Ti/Au) on the left. Current  $I$  is measured after passing through Al superconductor (blue shell on top of nanowire). InAs (green) is the bare nanowire that becomes an insulator when*

gate voltage  $V_{BG}$  is applied to the doped silicon layer underneath (dark background).

Once a device is fabricated and set up for measurements in a cryostat, the primary control knobs available to the authors are source-drain bias voltage between normal and superconducting contacts, gate voltage(s), external magnetic field (or magnetic flux) and temperature.

The two additional measurement techniques used in the Science-2020 paper are supercurrent through the shell (Figure 1) and Coulomb blockade (Figures 6 and 7). Figure 1 does not show Majorana measurements and is redundant with respect to Figure 2 for the purposes of our analysis. Figures 6 and 7 (Coulomb blockade measurements) are secondary to data in Figure 2, meaning that irreproducibility of Figure 2 cannot be rectified by data or analysis in Figures 6 and 7. We will make further comments on the Coulomb blockade technique below after presenting our analysis. Figures 3, 4 and 5 are devoted to theory, which is not relevant to how representative the tunneling data are. We comment on the theory later.

### 3. Analysis of tunneling data (Figure 2)

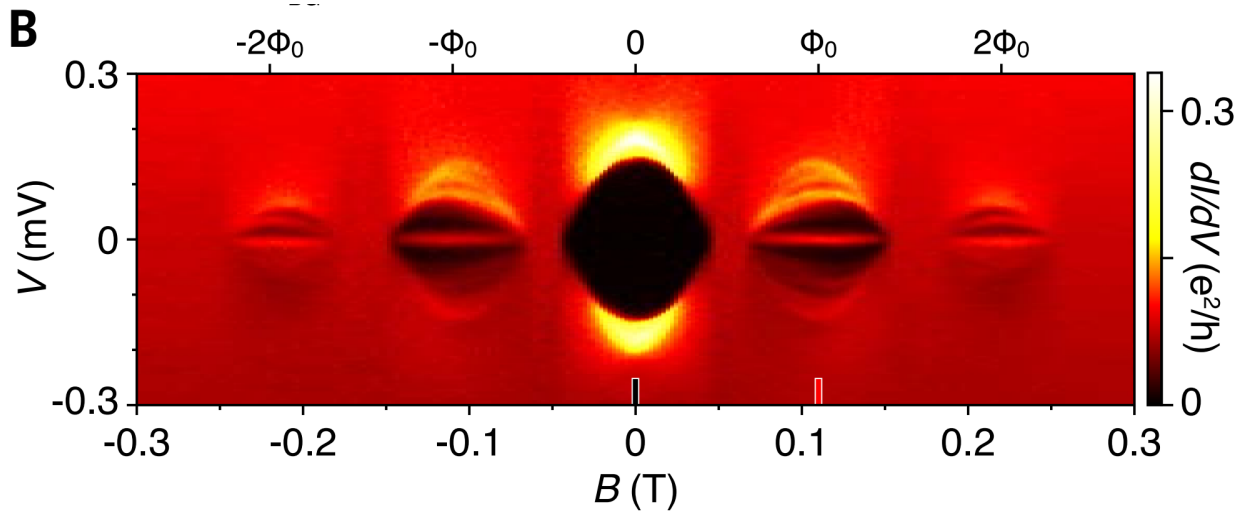


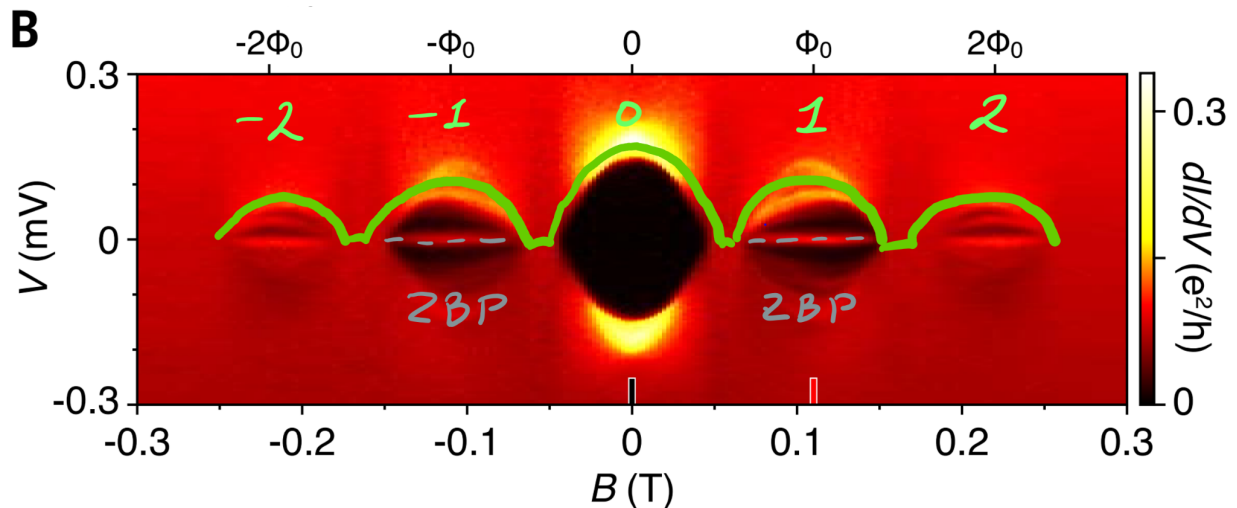
Figure 2 is composed based on three separate datasets, panels B, C and E, all presented as colormaps of conductance  $dI/dV$ , given in the units of  $e^2/h$ . Panel B is the most illustrative and the most discussed in the paper, it is a magnetic field  $B(T)$  evolution of conductance as function of source-drain bias voltage  $V(mV)$ .

Panel 2B presents two key phenomena. The first of them is the zero-bias peaks that we mark with gray dashed lines below. They are visible at  $V = 0$  mV and around  $B = 0.1$  T and  $B = -0.1$  T as two narrow and long red horizontal streaks surrounded by a dark

background. The second is the oscillations of the dark, low conductance region around zero voltage bias that we marked by the green trace. They have been known since 1962 as Little-Parks oscillations in superconducting rings. The lobes of oscillations correspond to the number of flux quanta threading the nanowire which we label with green numbers -2, -1, 0, 1, 2. The top horizontal axis labels magnetic flux in units of flux quantum  $\Phi_0$ . Important for understanding the authors' statements is that each flux quantum corresponds to the winding of the superconducting wavefunction's phase of  $2\pi$ , a flux of  $2\Phi_0$  is  $4\pi$  winding, etc. This language of 'winding' is used in the paper.

The relationship between the two phenomena, zero-bias peaks (ZBP) and Little-Parks oscillations (LP) is the topic of the Science-2020 paper. The authors use Little-Parks oscillations as a counter for how many flux quanta are threading the wire. This number of flux quanta they connect to topological superconductivity (MZM):

*"We show experimentally and theoretically that the winding of the superconducting phase around the shell induced by the applied flux gives rise to MZMs at the ends of the wire."* From the Structured Abstract, also referred to as the Research Article Summary.



Also from the main text:

*"The topological phase sets in at relatively low magnetic fields ( $\sim 0.1$  T), is controlled discretely by moving from zero to one phase twist around the superconducting shell"* Science-2020, p1.

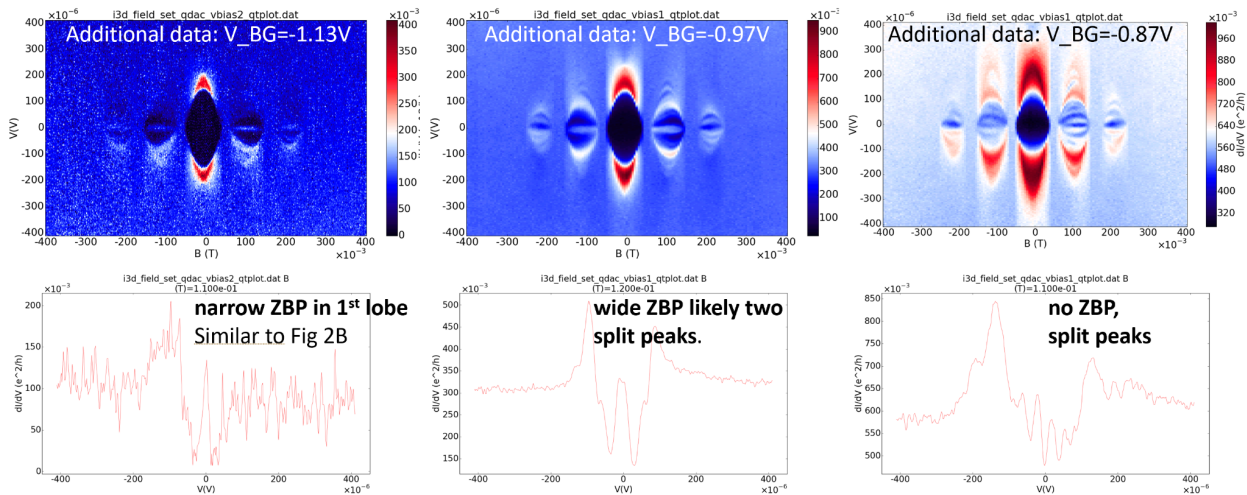
And here is an example of how the authors describe this relationship in more technical terms, relating zero-bias peaks to the first lobe of Little Parks oscillations (LP-1):

*“In the superconducting regions around one quantum of applied flux, corresponding to phase twists of  $\pm 2\pi$  in the shell, tunneling spectra into the core show stable zero-bias peaks, indicating a discrete subgap state fixed at zero energy.” Science-2020, p1.*

In Appendix A we list 30 instances where the relationship between ZBP and LP is stated in Science-2020, including 7 that discuss the reproducible coincidence of ZBP and the first lobe of the LP (LP-1). In what follows we analyze the ZBP/LP-1 coincidence itself and do not contribute any of our own interpretation of its relationship to the topological/Majorana physics. (We also analyze several other statements that the authors make about there being no subgap features in LP-0 or the even/odd pattern. Those statements are important but secondary to the coincidence of ZBP and LP-1.)

Figure 2 presents data from Device 1, and shows a clear coincidence of the ZBP with LP-1. To understand how reproducible this is, we first turn to additional data from the same Device 1; these data were not published with the Science-2020 paper. We replot these data from Zenodo files, hence the different colorscale.

We see three additional datasets, the difference between them is the setting of back gate voltage  $V_{BG}$ . Only one of the new datasets,  $V_{BG} = -1.13$  V, shows a narrow ZBP comparable to panel 2B. At  $V_{BG}=-0.87$ V we see no ZBP in LP-1. Instead, peaks at finite  $V$  (also referred to as split peaks) are observed.



At  $V_{BG}=-0.97$ V (center) we see a ZBP which is thicker in voltage bias. Continuing the trend from data at  $V_{BG}=-0.87$ , this thickening of the peak can be a consequence of having not a single ZBP but two closely spaced and overlapping split peaks. This is also

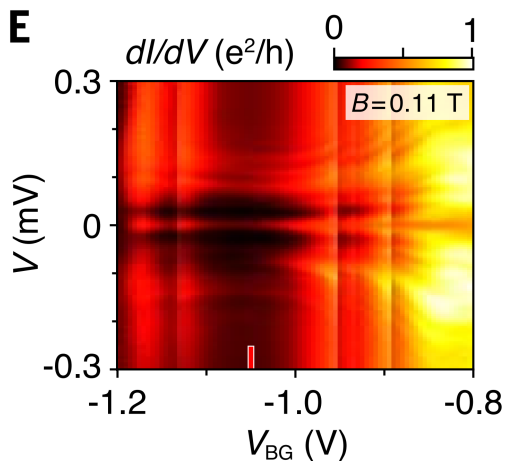
confirmed by the additional back gate voltage dependence data shown in the next section.

### 3.2 Gate-dependent zero-bias peaks

Additional data reveal that the presence/absence of ZBP is related to how the back gate voltage is chosen. This is seen in the magnetic field dependences presented above, and in the additional gate voltage dependences plotted below. The fact that gate voltage can control ZBP should be surprising to a reader of the paper. The authors state:

*“Although full-shell wires do not allow for direct gating of the electron density in the semiconducting core, we demonstrated that, using a careful design of the wire properties—for example, by choosing the appropriate radius— it is possible to obtain wires that harbor MZMs at a predictable magnetic field”*

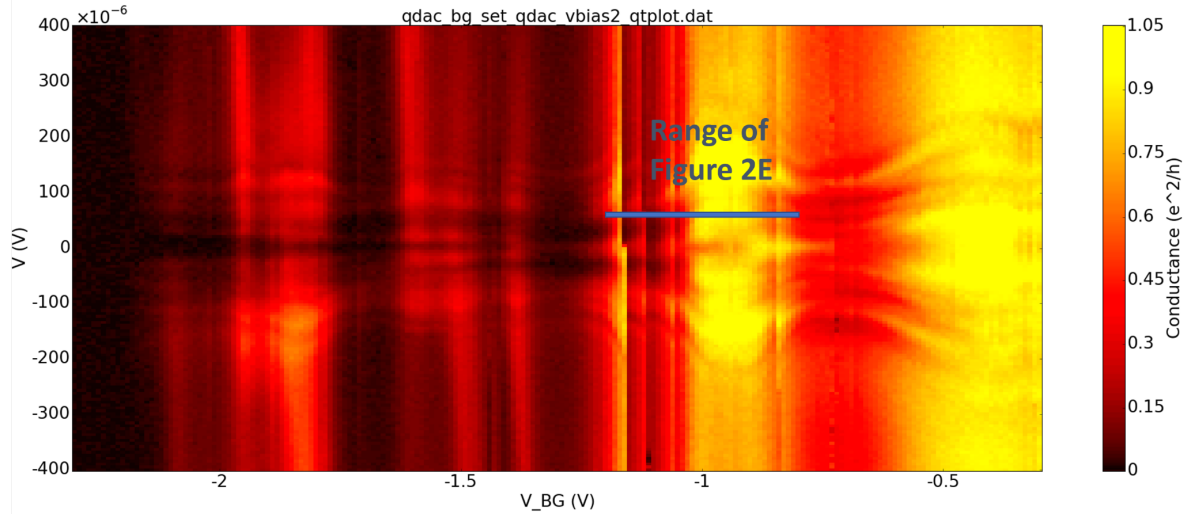
While lack of gating of the inner core of the wire is stated in the paper and is reasonably expected from a device clad in a full metallic shell due to screening, the actual measurements related to gate sensitivity of ZBP are shown in Figure 2E, which is the back gate evolution of conductance, now at a fixed magnetic field. This is how data in panel 2E are described in the text:



*“In the first lobe, at  $B = 110$  mT, the sweep of VBG showed a zero-energy state throughout the tunneling regime (Fig. 2E). [...] As the tunnel barrier is opened, the zero-bias peak gradually evolves into a zero-bias dip.”* Science-2020, p2.

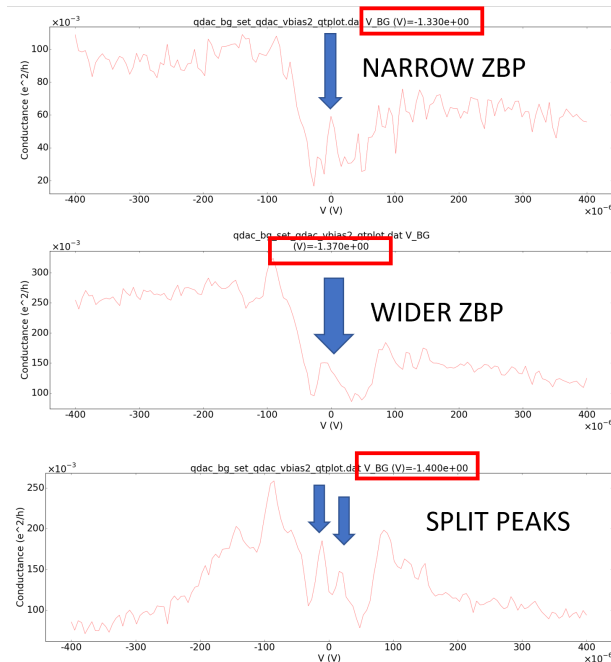
Indeed, in Figure 2E we see a zero-bias peak that spans most of the image. The ‘dip’ observed around  $V_{BG} = -0.8$  V is also interpreted by the authors in the context of MZM (more on this later). Thus, the entire panel E is associated in the paper with the topological regime.

However, in contrast with Figure 2E, additional data contain a dataset over a larger range of  $V_{BG}$  with a ZBP region similar to that in Figure 2E but which covers about 18% of the full gate voltage range. The additional data in the image below do not show 1:1 correspondence to the data in Figure 2E, presumably due to irreproducible charge jumps. To establish some correspondence with Figure 2E, we mark the gate voltage range of the Figure in the plot of additional data.



After replotting and analyzing these data, we find the following regimes:

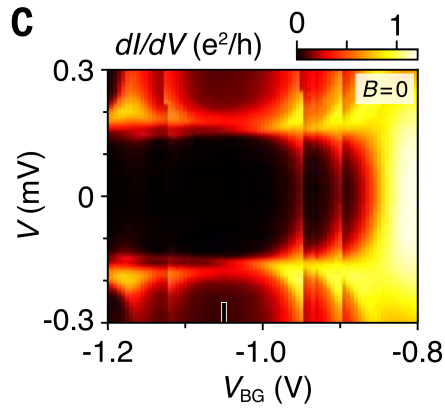
- 1) Noise without features between  $V_{BG} = -2.25$  V and  $-2.19$  V
- 2) Split peaks between  $V_{BG} = -2.19$  V and  $-1.38$  V (does not appear in Figure 2E)
- 3) ZBP between  $-1.38$  V and  $-1.035$  V (similar to Figure 2E)
- 4) Split peaks between  $-1.03$  V and  $-0.90$  V (similar to Figure 2E, and also where the magnetic field dependence shown in the previous section at  $V_{BG} = -0.97$  falls, though gate voltages may not correspond to each other due to irreproducible charge jumps)
- 5) ZBP between  $-0.90$  V and  $-0.70$  V (does not appear in Figure 2E)
- 6) More split peaks between  $-0.7$  V and  $-0.3$  V (does not appear in Figure 2E)



Thus, additional data of gate voltage dependence in LP-1 demonstrate regions of split peaks that exceed in gate voltage range the regions of zero bias peaks, and a second region of zero bias peaks at more positive gate voltages. This contradicts statements in the paper regarding the gate voltage dependence of zero-bias peaks.

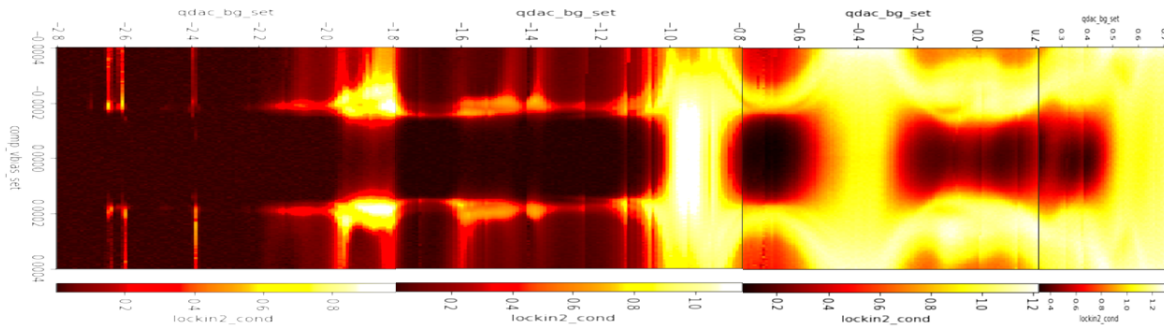
We observe that the zero-bias peak never approaches the noise level in this additional dataset. It remains visible until it is replaced by a pair of split peaks. The splitting is gradual, as far as linecuts show.

The description of Figure 2E contains the phrase ‘*throughout the tunneling regime*’. Science-2020, p2. We understand this phrase as the range of  $V_{BG}$  in Figure 2E (and 2C) being the only relevant range. The ‘tunneling regime’ is the regime where



conductance at finite bias, e.g.  $V > 0.3$ , is below 2 at zero magnetic field, and below 1 at large magnetic field. Figure 2E is composed in such a way that at the left boundary of the panel the overall conductance is low, 0.1-0.3, and at the right boundary of the Figure conductance is high, approaching 1. The same impression is given by panel 2C which is the same regime as 2E but at zero magnetic field.

The statement that the entire tunneling regime has been presented in Figures 2E and 2C can be scrutinized by considering the additional data obtained at zero magnetic field (this is a composite of four separate datasets, the range of Figure 2C is between -1.2 V and -0.8 V):



From these data, not published with the Science-2020 paper, we see that:

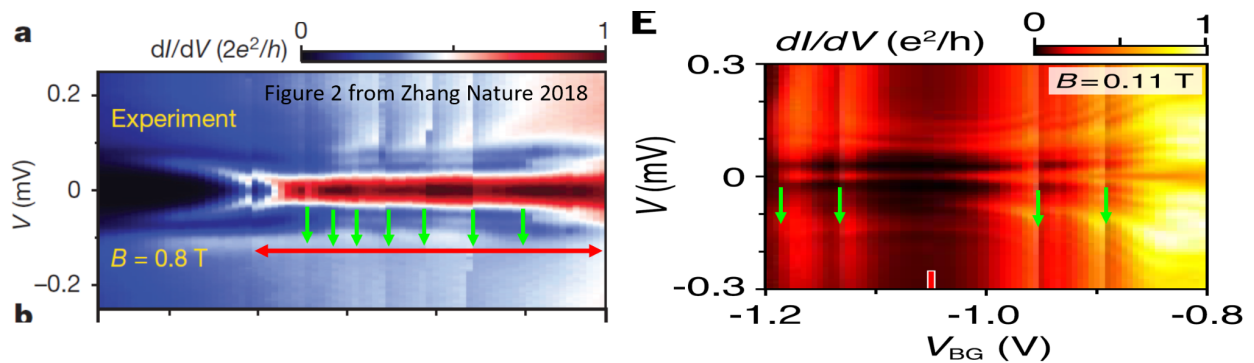
- 1) Conductance is below 1 at high  $V$  (e.g. top edge) for back gate voltages as high as  $V_{BG} = +0.2V$ , outside of high current resonances (vertical yellow streaks). At zero magnetic field, tunneling takes place for conductances below 2 in the basic picture.
- 2) The superconducting gap feature (horizontal peaks at  $V = \pm 0.002$ ) are present for back gate voltages as low as  $V_{BG} = -2.7V$ , indicating that electronic tunneling is still taking place.

From this we conclude that a much larger back gate voltage range  $-2.7V < V_{BG} < +0.2$ , or larger, corresponds to the tunneling regime. The data in Figures 2E and 2C, over the gate voltage range between -1.2 V and -0.8 V occupy only a fraction of the tunneling regime. Consequently, the statements in the paper that zero-bias states are

observed throughout the tunneling regime are incorrect, since in other parts of the range split peaks are observed.

We stress that the argument we make does not boil down to a debate about the appropriate gate voltage extent of the tunneling regime. The need to have presented a larger range of gate voltages within the paper, so as to make it clear that gate voltage does have a significant effect on the apparent zero-bias peak, is only made stronger by the uncertainty in determining which range corresponds to the tunneling regime. The authors did not present these data, but instead put statements in their paper to suggest the absence of gate effect over a relevant gate range. The possibility that this is not the full relevant gate range was not presented.

The gate voltage range with ZBP that was shown in Figure 2 is extended by ‘charge jumps’ which are sharp discontinuities in the colormap. As the back gate voltage increases the signal shifts back to a previous value, in a manner similar to a skipping record, but due to a shift in the position of a small charged particle near the nanowire. Charge jumps were used in a recently retracted ‘Quantized Majorana Conductance’ Nature paper, originally published in 2018, to extend the gate voltage range of ZBP (green arrows):

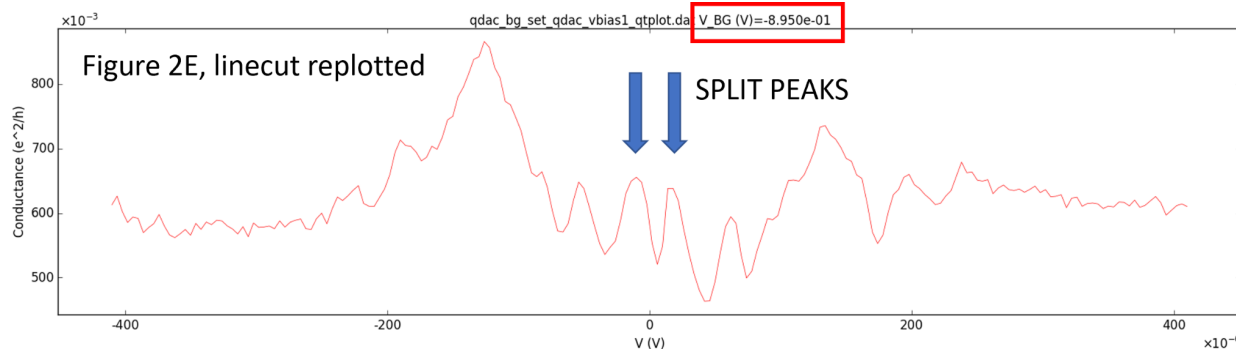


We furthermore find that the following sentence from Science-2020 is inaccurate. It is important to point out this inaccuracy because the statement connects a feature of the data to a ‘theory supporting MZMs’:

*“As the tunnel barrier is opened, the zero-bias peak gradually evolves into a zero-bias dip. The increase of finite-bias conductance compared with zero-bias conductance as tunnel barrier decreases is in qualitative agreement with theory supporting MZMs” p2.*

The inaccuracy occurs where the authors discuss the evolution from a zero-bias peak to a zero bias dip. In fact, the zero-bias peak splits and becomes two peaks. We replotted Figure 2E ourselves to verify this, and we can also see from additional magnetic field

sweep data, as well as from additional gate voltage sweep data, that these are not dips but rather a pair of peaks, split away from zero bias voltage to a finite positive and finite negative voltage, symmetric around zero bias voltage.



At more positive gate voltages an apparent dip can indeed be seen at zero voltage bias. However, where the authors make a link to an MZM theory they do not discuss or explain how split peaks fit into this comparison between experiment and theory. We find this to be significant based on our understanding of the cited and other MZM theories.

To summarize our analysis of available tunneling data for Device 1 (Figure 2 vs. additional data) we conclude that both the magnetic field dependence (panel 2B) suggestive of correlation between ZBP and LP-1, and the gate voltage dependences (panels 2C and 2E) suggestive of zero-energy states present throughout the tunneling region of back gate voltage are not representative of the total data. This leads to statements in the text of the paper, where these data are described and generalized, to be invalid.

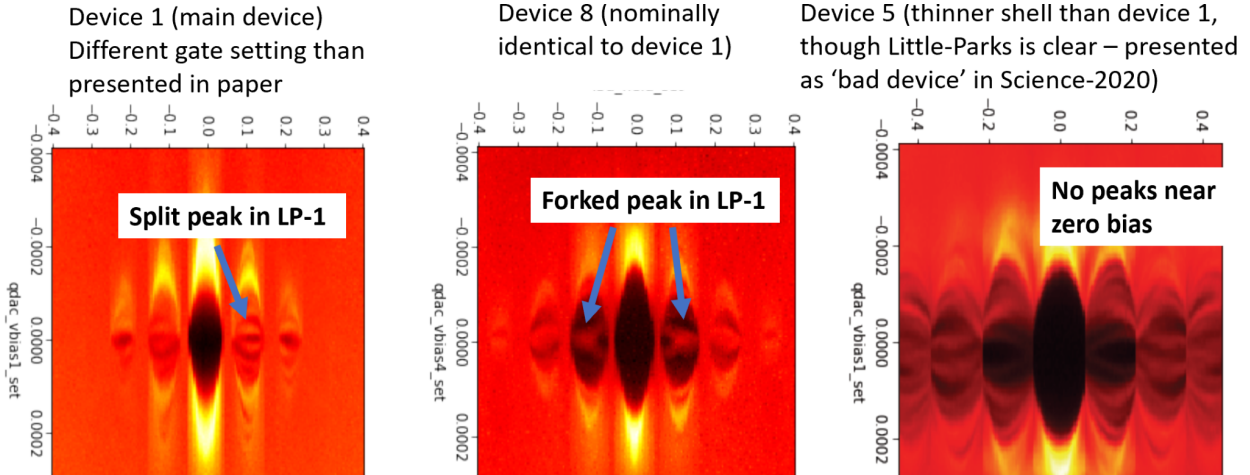
#### 4. Device-to-device reproducibility

An important part of the argument that the authors make in their Science-2020 paper is reproducibility of these observations from device to device. They write:

*“Two device geometries, measured in three devices each, showed similar results.” Science-2020, p1.*

*“Moreover, the full shell naturally protects the semiconductor from impurities and random surface doping, thus enabling a reproducible way of growing many wires with essentially identical electrostatic environments.” Science-2020, p6.*

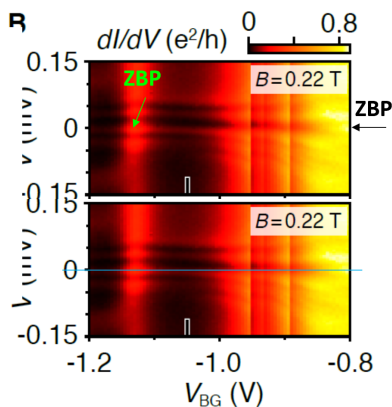
The total number of devices for the tunneling geometry was subsequently disclosed by the authors to be 9. We can compare data from those devices to Figure 2.



On the left we repeat data from Device 1, not shown in Science-2020, where no ZBP is observed in LP-1. In the center, we see data from Device 8, not shown in Science-2020, which authors describe as ‘nominally identical’ to Device 1. We see that within LP-1 a pair of split peaks merge into a ZBP, a behavior which suggests that there is no connection between the phenomena of LP and ZBP in this case. On the right, we see data from Device 5 which the authors describe as different from Device 1, a statement that does not find strong support in additional data (more on that later). In this device, while LP oscillations are clear, we see no ZBPs.

Some datasets from other devices, 3, 4 and 9, do show a coincidence between ZBP and LP-1 in magnetic field sweeps, in line with Figure 2B. However, as we demonstrate above for Device 1, this can be a result of acquiring data at an atypical setting of gate voltage where such coincidence appears. Recall that from each device we only see a few datasets on Zenodo. Taken together, additional data and paper data provide plenty of examples where the relationship between ZBP and LP-1 is either present or absent. However, Figure 2 of the Science-2020 paper itself only shows that the two phenomena coincide.

#### 4.2 Even/odd pattern



The authors extend and generalize their experimental statements beyond the LP-1 coincidence. They suggest that whenever the number of flux quanta is even, 0 or 2, there is no ZBP. But when the number of quanta is odd, 1 or 3, there is a ZBP. This fits with their MZM narrative, and they make at least 20 statements throughout the paper, where they indicate that their data support this ‘even/odd’ pattern. We list the statements in Appendix A. We do not

find support for the existence of such an even/odd pattern in the total data we considered.

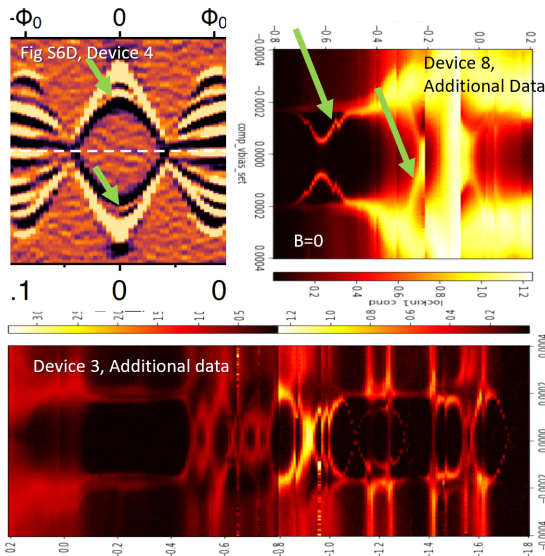
The data to support the entire even/odd ZBP/LP pattern in a single graph is limited to one dataset from Device 4 that shows a pattern up to LP-3. However, in Device 3, the key verification device, and in Device 12, nominally identical to Device 1, there are no ZBPs in LP-3. In fact, the only dataset from Device 12 shows no peaks in any lobes. In Device 5, the ‘bad’ device which has no ZBPs in LP-1, we see broad ZBPs in LP-3. In other devices LP-3 is not visible.

The even/odd pattern would imply that no ZBP is present in LP-2. However, we find for Device 1 a zero-bias peak in the gate voltage dependence within LP-2. This contradicts this statement in the supplementary materials:

*‘In the second lobe, with even number of phase windings, the spectrum for device 1 features an asymmetric superconducting density of states with the lowest energy subgap state centered around  $\sim 5$  ueV, see Fig. S3.’ SM, p3.*

To illustrate this statement, the authors present a magnetic field dependence focused on LP-2 at the back gate set to  $V_{BG} = -1.05$  V. The zero-bias peak in Figure S3B is at  $V_{BG} = -1.15$  V, a different back gate voltage.

#### 4.3 Empty gap within LP-0 (near zero magnetic field)



A statement regarding LP-0, repeated with variations several times in Science-2020, is stronger than the even/odd pattern would imply (i.e. no ZBPs in LP-0). The statement is that no subgap states at any bias are present in LP-0:

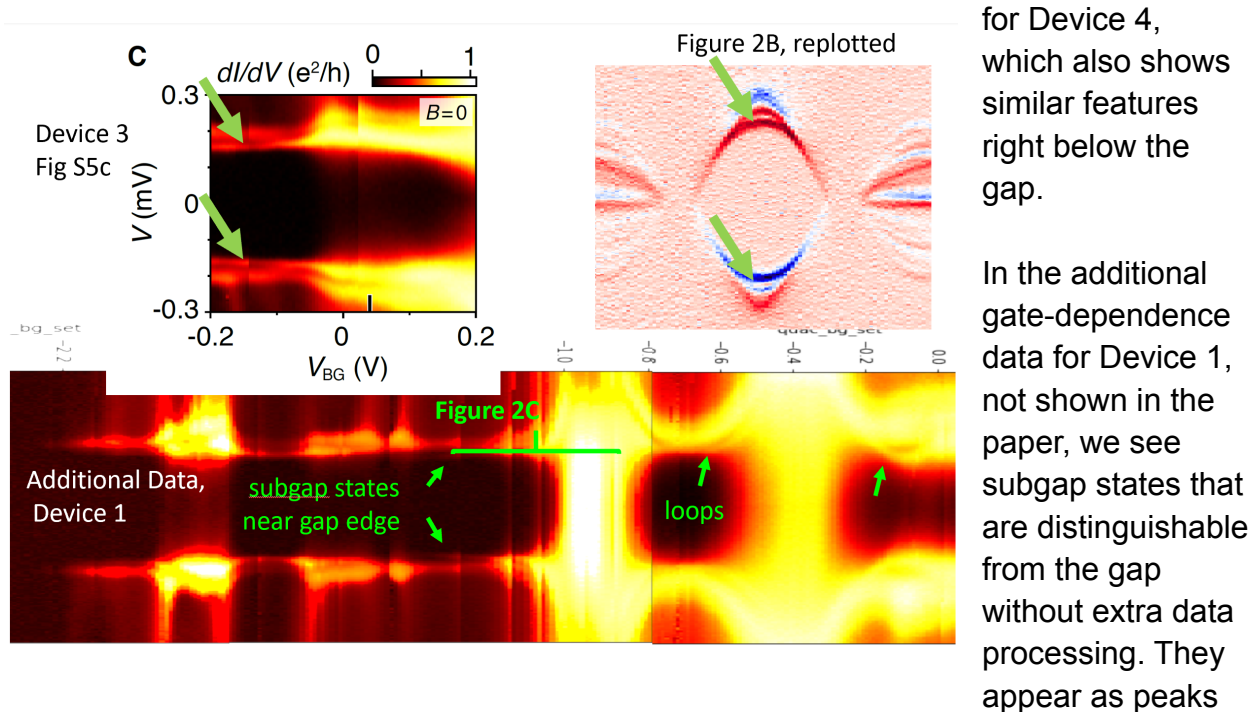
*‘Our measurements reveal that tunneling into the core in the zeroth superconducting lobe, around zero flux, yields a hard proximity induced gap with no subgap features.’ Science-2020, p1.*

The importance of the statement of ‘no subgap features’ in LP-0 for the narrative of the paper is high. If there are subgap

features in LP-0, it leaves the possibility open that these features shift to zero energy in magnetic field due to its Zeeman/orbital effect, rather than ‘discrete phase winding’. The notion that ZBP in LP-1 appears ‘out of nowhere’ would then tilt a reader towards believing that a discrete value of magnetic flux, within LP-1, is what generates that zero-bias peak.

Contrary to the statement above, we find in devices 1, 3, 4, 5, 8, 9 subgap features at zero magnetic field. The features are marked with green arrows for devices 1, 4 and 8. In Device 3, the states are so numerous that it is not practical to mark them all.

In Device 4, and in the main Device 1, which is the basis for Figure 2, we identify subgap features that happen to be located very near the edge of the gap. As a reminder, ‘the gap’ is a horizontal peak in the back gate voltage dependence at approximately  $\pm 0.0002$  V. We notice that these subgap features exist for those gate voltages that are used in Figure 2. In Figure 2 these are not apparent, and only can be identified if an additional data processing step is taken. In the replotted Figure 2B we take a numerical derivative in the vertical direction to identify a feature near zero field. This numerical derivative is the same procedure that the authors applied in Figure S6D



for Device 4, which also shows similar features right below the gap.

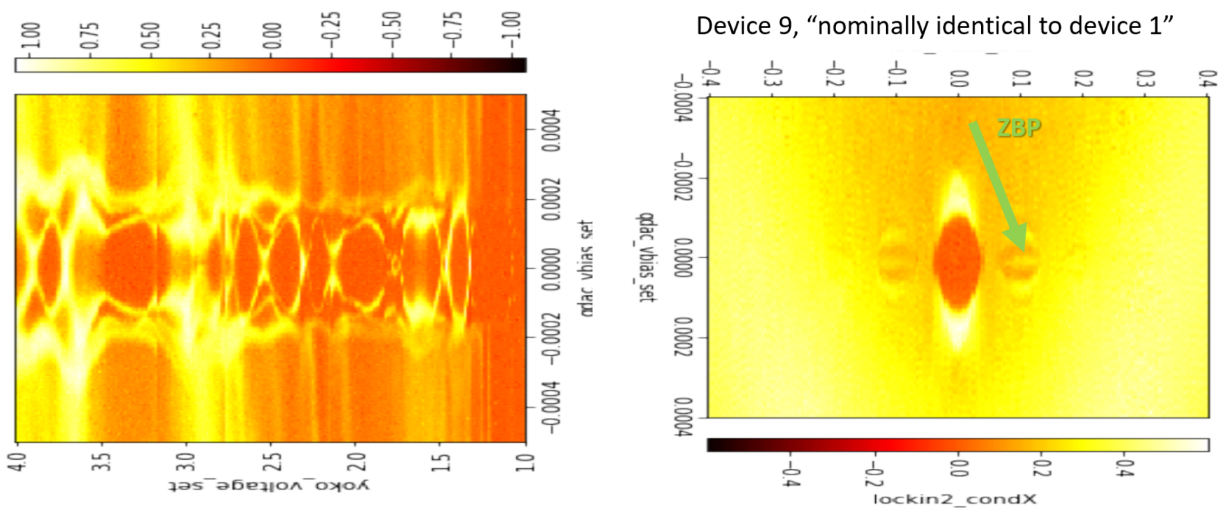
In the additional gate-dependence data for Device 1, not shown in the paper, we see subgap states that are distinguishable from the gap without extra data processing. They appear as peaks

at different  $V$  values than the gap. These subgap features appear either as peaks that track along the gap for a range of gate voltage, or as half-loop resonances. The gate voltage range of each of the two loops is greater than 0.2 V, a range comparable to the entire gate voltage range of Figure 2C, 2E.

The fact that the existence of subgap features was not disclosed or discussed in the paper, regardless of their ultimate origin which cannot be unambiguously elucidated based on the available data, is significant. Statements about LP-0 made in the paper lose part of their support and become either inaccurate or misleading.

#### 4.4 More examples illustrate the large variety of observed phenomena

Device 9, revealed with additional data and referred to as ‘nominally identical to device 1’, shows that it is possible to see a ZBP correlated with LP-1 in a device that, at zero magnetic field, contains numerous states that are not confined near the gap edge, but instead cross  $V=0$  throughout the gate voltage range. Thus, additional data also demonstrate that a zero-bias peak can be observed in the presence of ubiquitous subgap features. This raises further questions about the correlation of LP-1 and ZBP and how the data might look in other regimes not presented in the paper or in the additional data.



Device 8 offers another illustration that a wide range of behaviors has been observed in the authors’ experiments, and the coincidence of ZBP and LP-1 is not a representative behavior. At zero magnetic field, Device 8, nominally identical to device 1, exhibits two features, one a resonance that does not cross  $V=0$ , and appears at gate voltage  $V_{BG} = -0.3$ . Another one is a resonance that does cross  $V=0$  at  $V_{BG} = -0.2$  (a charge jump at the same gate voltage makes it harder to see). The authors set  $V_{BG}$  in between the two resonances (blue line), presumably in order to avoid them. However, when the magnetic field is turned on we see a fork-like resonance in LP-1: a pair of peaks merging into ZBP only half way through LP-1.

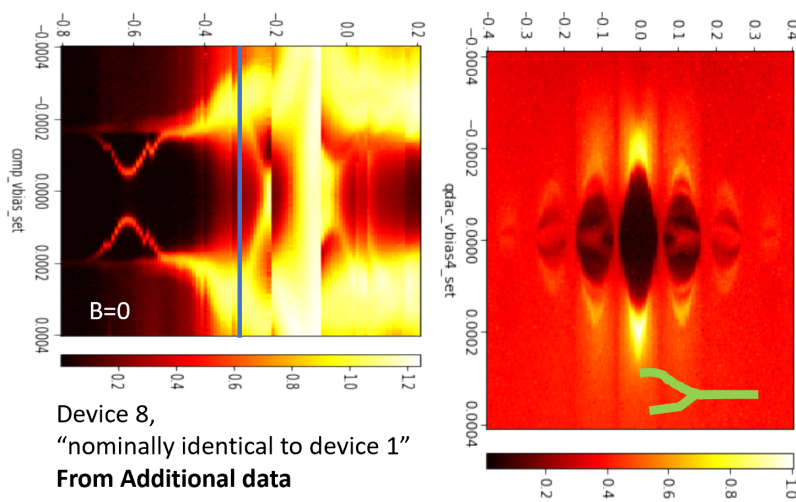
This is another example of possible behavior of subgap resonances. It is likely that if more magnetic field sweeps datasets were provided to us, e.g. at different gate voltages, more examples would be collected showing a rich variety of behavior, but not a correlation between ZBP and LP-1. It is possible that the authors already have more data like that, in which case they should share these data. At the very minimum, additional data demonstrate a range of phenomena that greatly exceeds those presented in the Science-2020 paper.

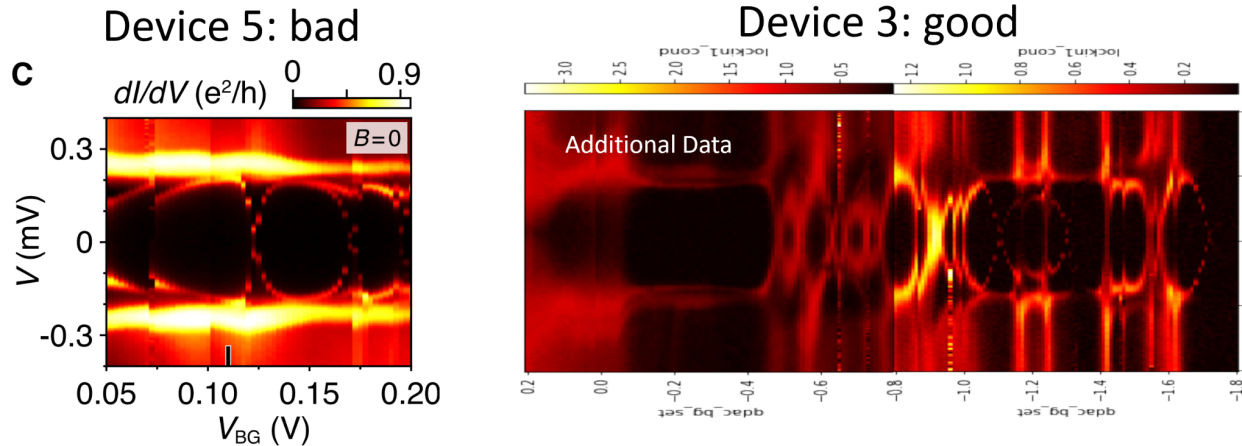
#### 4.5 Device 5: “bad” device with no ZBP but with Andreev Bound States

The authors present a device in the Science-2020 paper, Device 5, for which they do not show data with ZBP in LP-1. They explain the difference between Device 5 and other devices (1, 3, 4) as due to a thinner shell of Al, and/or thicker nanowire diameter in Device 5. We refer to Device 5 as ‘bad’ and to Devices 1, 3, 4 as ‘good’, with the meaning that ‘bad’ devices do not show ZBPs.

There is no evidence provided that the absence of ZBP is due to differences in the nanowire geometry. But we find even more significant the fact that Device 5, for which ZBP is not shown, is the only device for which the paper acknowledges the presence of subgap resonances in LP-0. This is how the authors describe them:

*“For device 5, a discrete state crosses zero-energy around VBG = 0.12 V and then again at 0.17 V, resembling a proximitized quantum dot state, similar to the one previously studied in Ref. [84], see Fig. S7. We usually associate such state with a resonant level in the barrier and if possible avoid it in the measurements.” SM, p3.*





A ‘proximitized quantum dot state’ is another name for an Andreev Bound State (ABS). As a reminder, Andreev Bound States are a widely known explanation for zero-bias peak, which is potent because these states can appear over parameter ranges much larger compared to MZM. A reader might infer that Andreev Bound States were only found in this ‘bad’ Device 5. But as we already demonstrated, subgap features, some of which are likely Andreev Bound States, are visible in many Devices.

To illustrate this, we show side-by-side with data from Device 5, an analogous dataset from Device 3. In contrast to Device 5, which is a ‘bad’ device with ABS and no ZBP, this Device 3 plays a role of the verification device in the paper. Meaning, this is a ‘good’ device that is used to show that the findings from Device 1 can be reproduced. As we see from the data shown above, Device 3 is actually similar to Device 5. Both exhibit multiple subgap features that cross  $V=0$ . This can only be seen in the additional data for Device 3, and not in the Science-2020 paper, where the authors select regions with only subgap features near the gap edge, and not the ones that reach  $V=0$ , for supplementary Figure S5.

## 5. Discussion of the paper text and other figures

After the paper’s figures, the main text of the paper is the most important factor in how the scientific claims are perceived by readers of the published paper, and before them by referees and editors when weighing the paper for publication. We already presented a case that individual statements from the main and supplementary text are incorrect. Here we discuss the paper as a whole.

In the experimental part of Science-2020, data descriptions as well as data interpretation are presented in simple and non-nuanced fashion. They project

confidence in conclusions and stand in contrast with the complexity of phenomena revealed in additional data.

It is especially striking that an alternative explanation of ZBP, in terms of Andreev bound states or related phenomena, is absent from the main paper text entirely. No mention of this possibility is made in the text. Out of 82 references, only a single theoretical paper (Ref 75) deals with Andreev ZBPs, but the paper is not cited in this context. No experiments that demonstrate a ZBP due to non-Majorana origins are referenced. Contrarily, 6 experimental articles are referenced interpreting zero bias peaks through the Majorana hypothesis.

A reader is not informed of the alternative explanation, and if they know about it, their mind is directed away from it. An example of such misdirection is the description of Device 5 which shows Andreev bound states in supplementary materials, where this device is explained as distinct from Device 1 due to different nanowire cross-section. It is dismissed using confident language but without evidence, based on speculation.

Distinguishing the Majorana hypothesis from the Andreev hypothesis is the main task in this research community when conducting experiments. The authors are well aware of widely discussed trivial zero-bias peaks due to Andreev bound states. They know about this from literature (first published in 2014), conferences (first presented in 2013) and many personal interactions. The 2016 Science paper from the same experimental group (Deng et al, Science 2016) discusses Andreev and Majorana states together. Most recently, the authors confirmed their awareness of the Andreev interpretation in April 2021 in their response to a previous version of this analysis.

If there is an alternative explanation, established for many years, at the very least this urges caution and extra rigor in making an ambitious Majorana claim in a high-impact journal. It should not be enough to offer a mere possibility that experiments may have a connection to Majorana, and ignore substantial evidence that the optimism is not based on reality. It should not be enough to show only a few datasets to substantiate your conclusion. Any Majorana theory provides plenty of opportunities to check and cross-check the experiment. After obtaining an interesting zero-bias peak, it is possible to further verify whether any given ZBP it is due to Majorana or if it is just an example of fine-tuned Andreev states by e.g. repeating magnetic field sweeps for a large number of different fixed gate voltages. This type of cross-check is at the core of our analysis, and it shows that multiple claims within the paper are inconsistent with the data.

## 5.2 Comments on the theory part

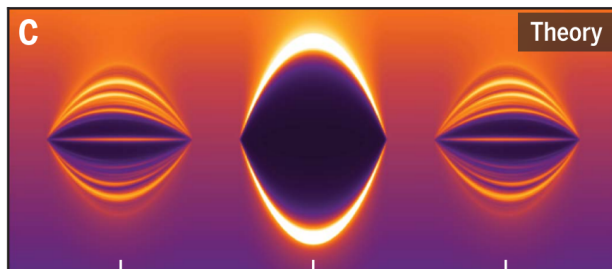
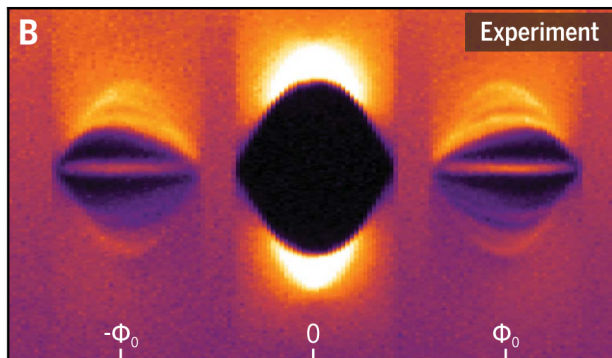
Science-2020 paper contains an equal theoretical contribution, to which Figures 3,4,5 are dedicated. Originally, the theory part and the experimental paper were separate papers: they were posted on arXiv under separate identifiers (1809.05513 and 1809.05512). There was no overlap in the list of authors between the theory paper and the experimental paper. A version published in Science-2020 combined the author lists. The content of the two papers also got combined. Its two cores remain similar, meaning that the arXiv posting of the theory paper has strong overlap with the theory part of the joint Science-2020 paper.

We contend that the fact that the experimental part dedicated to the tunneling technique contains multiple incorrect statements, and its experimental conclusions where data are concerned are not supported by additional data, makes the Science-2020 paper invalid, in the form it was published (i.e. joint with the theoretical part).

There is therefore no need to consider the theory part in great detail. We limit our discussion to only a few remarks.

First, the theoretical model shows that ZBP correlated with LP-1 can appear in the topological regime, as well as in the non-topological regime (Figure S23). Whether this observation has any relationship to the experimental part is unclear, since theory considers an idealized model of the device. Nevertheless, the discussion of Figure 23

appears to be in direct contrast with the discussion of Figure 2 where no such possibility that a ZBP correlated with LP-1 need not be related to a topological state, is presented.

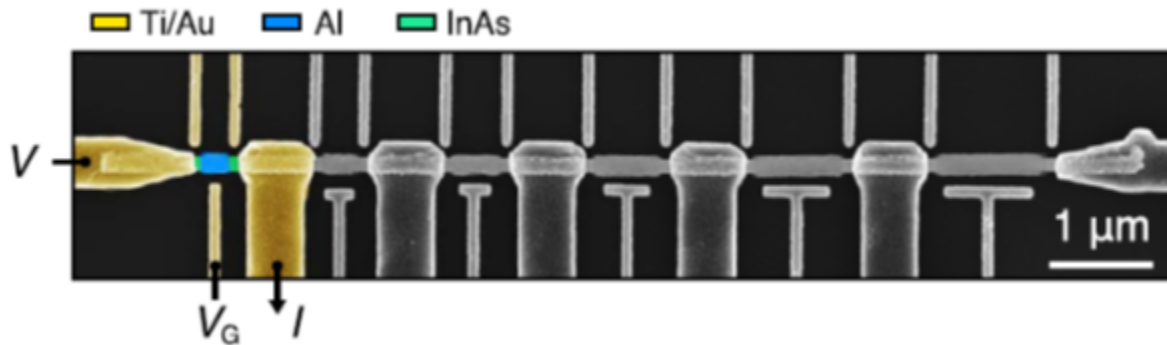


Second, and despite the fact that the theory is weak at associating ZBP with MZM, Figure 5 shows numerical simulations that closely resemble Figure 2. They are highly suggestive of a good match between experiment and theory. These simulations serve to convince a reader that theory does, in fact, provide strong support for the MZM explanation of the experimental data. As stated above, this is not the case.

Third, the theory part also makes a connection to the Coulomb blockade part of the paper, which we comment on below. The theory suggests that an ‘exponential scaling’ of the parameter extracted from the Coulomb blockade (peak oscillation amplitude) is indicative of the topological regime and is a better predictor of this regime than the coincidence of ZBP and LP-1. We have doubts about the experimental methodology of the CB technique, and about the relevance of the parameter extracted from it. The strength of the exponential scaling argument is also unclear. Devices of different length are different realizations of a system and to make a strong statement about scaling, it is necessary to generalize the observations by performing a lot more simulations. The question of how well the model describes the experimental system and whether another model cannot produce exponential scaling without MZM is an open question.

### 5.3 Comment on Coulomb blockade section

The authors present another experimental technique based on measuring spacings of the so-called Coulomb peaks. Figures 6 and 7 are dedicated to this technique. Similar to our argument for not considering the theoretical part, we do not see a reason to consider the Coulomb blockade part. Since Figure 2 and its description misrepresent full data and contain serious errors, any arguments contributed by an additional technique do not change the fact that the paper is invalid. However, we will make several broad remarks about the Coulomb blockade technique.

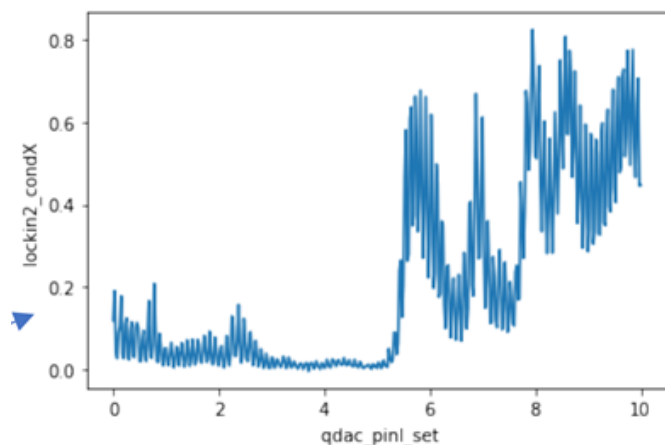


Coulomb Blockade (CB) measurements on small superconducting islands are not widely used in Majorana studies. Other groups studied such devices. But only the Copenhagen-Microsoft group made Majorana observation claims based on this measurement technique, in papers such as Albrecht et al. Nature 2016, Sherman et al. Nature Nanotechnology 2017. We find several aspects of this technique questionable, and we are interested in re-analyzing all of the papers that use it for Majorana explanations, in a separate study.

Figures 6 and 7 present data from Device 2, which is in fact 6 separate islands of AI of 6 different lengths. The results from all 6 islands are analyzed together as a length dependence of the topological regime. That means, each of the 6 nanowire segments contains MZM. Without looking at the data, let's cross-check this with what we already established from the tunneling technique.

We know that ZBPs, and hence Majorana modes, do not appear in every nanowire. Furthermore, finding a ZBP requires fine tuning of gate voltages. Based on this, it appears to be an unusually good device if it exhibits twelve Majorana zero modes, all at expected positions along the nanowire, at the ends of each AI island.

What is the likelihood of realizing such a device? If we assign a probability that a given segment has MZM to be 0.5, which we consider a high number, then the probability of having 6 segments is 1.5%. It would require, on average, 64 nanowires to find a single one like Device 2. If Majorana probability per device is  $7/9$  (which matches the authors' count of devices with ZBPs vs. total working devices), then the probability of 6 topological segments in one wire is 22%. The authors present not one, but three such nanowires, two more in additional data. The coincidence appears too good to be true.



The CB technique the authors use relies on calculating mean distances between even and odd Coulomb peaks. To extract peak distances the authors use positions of between 6 and 22 peak pairs. But in a wider range of gates, shown in additional data, we see of order 100 peaks, perhaps more.

What is not known is whether patterns shown in the Science-2020 paper persist over larger peak ranges? Do energy oscillations survive averaging over 100 peaks? Do oscillations look the same if different sets of peaks are averaged? The authors show in Figs S12, S15 that they can also change the back gate, and that it is set to a large negative value. Since NIS devices are highly sensitive to back gate, how do peak statistics change in the full range of back gate? Are there examples where scaling is not exponential? These are the types of questions we would ask if and when we embark on re-analyzing all of the CB technique papers. We have other, even more basic questions as well. We did not proceed with this analysis now because our finding

that Figure 2 is not representative of the devices studied is already sufficient to invalidate the conclusions of the paper.

#### 5.4 Comment on related results from Austria

Shortly after the Science-2020 paper was published, a preprint on arxiv from the IST group in Austria reported that in the exact same nanowires no Majorana modes are observed, but only trivial Andreev bound states (“Flux-tunable Andreev bound states in hybrid full-shell nanowires”, <https://arxiv.org/abs/2008.02348>). We do not base our post-publication analysis of the 2020 *Science* paper on this later preprint. We find that problems identified in Figure 2 and its discussion are significant enough to make the Science-2020 paper invalid. However, we comment on the IST results here anticipating a discussion of them may emerge.

The IST experiments show that the ZBP/LP-1 coincidence is a result of fine-tuning of the gate voltage settings. We conclude this based on a large volume of data, over 500 datasets, shared with us by the IST group.

The full-shell nanowires for both studies are grown by the same grower using the same growth equipment for both papers. Device fabrication including positioning of nanowires on silicon substrates, and deposition of electron-beam lithography patterned metal contacts (and gates) is generally similar. Though different cleanrooms were used to make devices, the processes appear to be not different in substantive ways. One way to see this is from the data themselves: devices from IST and Copenhagen exhibit similar low-temperature characteristics such as the induced superconducting gap, including its magnitude, hardness and its persistence in applied magnetic field; as well as similar Little-Parks oscillations that are specific to full superconducting shell nanowires.

The overall data quality is comparable, meaning that datasets of the same quality are present in the full IST data and in the Science-2020 paper, though they do not necessarily correspond to completely equivalent regimes. This however does not leave much room for claiming that the two studies are different in any significant way. Given the variety of data we found in additional Copenhagen data, we expect that full libraries of data show equivalent phenomenology.

#### 5.5 Summary of communications with the authors of the paper

We find communications with the authors to be a significant factor in our post-publication analysis, since explanations from authors have enormous potential to influence our understanding of their paper and their experiments.

To recap the history briefly, upon learning of the IST replication issues, we asked for the full data underlying the experimental claims in *Science*-2020. Initially the authors refused to provide it, insisting that all data necessary to reproduce their manuscript were available within the paper. They shared a limited amount of data after the *Science* editor intervened, after we sent a 10-page memo summarizing our concerns and questions (dated October 8). On finding that the additional data was not consistent with the paper, we asked the authors further questions along the lines of the analysis above. We did receive a response to our analysis from the authors. However, the response was not extensive or satisfactory. This precipitated this post-publication analysis, dated June 1 2021 in the original version, as well as publication of an Editorial Expression of Concern by *Science* on July 30 2021.

On July 26 2021 Jan Thomsen of Niels Bohr Institute informed *Science*, and shortly after a journalist at *Retraction Watch*, that the data shared by the authors on Zenodo constitute the entire body of experimental data and that 'No additional data is left out'. This is impossible; as we noted in our 10-page request for data dated October 8 2020. The volume of data for the tunneling (NIS) component of the study is 52 datasets total over 9 devices, or between 5 and 6 datasets per device on average. If this were all the data, then no scientific conclusion could be justified by such an insufficient study. Given the number of experimental variables to explore, the temporal instabilities in devices and the richness of phenomena present in those data made available, the required volume of study would need to be between 1 and 2 orders of magnitude larger. A comparison can be made with those experiments for which the volume of study is known. For instance, the volume of study for the IST-Austria *Science* paper is at least 500 datasets. While for the 2012 Delft *Science* paper on Majorana it is 4000 datasets. The pure data acquisition to obtain 52 datasets is of order 100 hours or less. Taking into account overnight data acquisition all the measurements could be accomplished in less than a week of pure measurement time, excluding fridge cooldowns. We find it highly unlikely that the entire duration of study was so short. We therefore doubt the assertion by Mr. Thomsen that this is all the data.

Assuming however that the statement of Mr Thomsen is correct, a study volume of 52 datasets over 9 devices is in itself grounds for a retraction of the paper. Parameters such as gate voltages and magnetic field are insufficiently explored to claim that any data presented in the Figures are robust. 'You try once, and go with whatever the screen shows' is not consistent with the scientific method. The richness of the obtained features would compel any experimental physicist to look further, not simply to repeat the same measurements but to vary parameters. For example, magnetic field dependences like those in Figure 2 should be studied for many different gate voltages,

in the regions that do not show zero-bias peaks. It is necessary to repeat gate voltage sweeps and many different magnetic fields, and to push the gate settings to establish where the true boundaries of the tunneling regimes are. Repeating these standard methods for each device of the 9 studied would result in a ten-fold or more increase in the volume of data, required to reach conclusions at the level of those presented in the Science paper.

More importantly, another implication of the statement by Jan Thomsen is that our original analysis from June 2021 is complete. If no further data can be forthcoming, then i we have taken into account the full volume of data, and our conclusions cannot be impacted by the appearance of previously unseen data that clarify or alleviate some or all of our concerns. Thus our previous conclusion, that the paper should be retracted, is further validated.

One thing we learned from the authors response is that they intended their paper to be merely suggestive of topological superconductivity. They also responded that they believe that “the topological phase can be present only in part of the 1st lobe and can also be present in the 2nd lobe.” While this may be consistent with the theory part of their manuscript, this is not how they described or represented the experimental data in the manuscript.

## APPENDIX A - Relevant quotations from the Science-2020 paper

### A.1 Statements about Majorana in the paper

1) *‘We show experimentally and theoretically that the winding of the superconducting phase around the shell induced by the applied flux gives rise to MZMs at the ends of the wire.’* Research Article Summary.

2) *‘The topological phase [...] is controlled by moving from zero to one phase twist around the superconducting shell.’* Research Article Summary.

3) *‘Two device geometries, measured in three devices each, showed similar results.’* p1.

4) *‘As the tunnel barrier is opened, the zero bias peak gradually evolves into a zero-bias dip. The increase of finite-bias conductance compared with zero-bias conductance as tunnel barrier decreases is in qualitative agreement with theory supporting*

MZMs...although the crossover from a peak to a dip occurs at lower conductance than expected.' p2.

5) 'Moreover, the full shell naturally protects the semiconductor from impurities and random surface doping, thus enabling a reproducible way of growing many wires with essentially identical electrostatic environments.' p6.

6) 'Although full-shell wires do not allow for direct gating of the electron density in the semiconducting core, we demonstrated that, using a careful design of the wire properties—for example, by choosing the appropriate radius— it is possible to obtain wires that harbor MZMs at a predictable magnetic field.' p6.

#### A.2 On tunneling spectroscopy at zero magnetic field:

1) 'Our measurements reveal that tunneling into the core in the zeroth superconducting lobe, around zero flux, yields a hard proximity induced gap with no subgap features.' p1.

2) 'At zero field, a hard superconducting gap was observed throughout the zeroth superconducting lobe (Fig. 2, B and D).' p2.

3) 'In a weak tunneling regime, for  $VBG < -1$  V, a hard gap was observed, with  $D = 180$  meV (Fig. 2, C and D). For  $VBG \sim -0.8$  V, as the tunneling barrier is decreased, the subgap conductance is enhanced owing to Andreev processes. The increase in conductance at  $VBG \sim -1.2$  V is likely caused by a resonance in the barrier.' p2.

4) 'A hard gap is seen in the zeroth lobe,...' and 'The zeroth lobe shows a hard superconducting gap,...' Fig. 2, commenting on data from Device 1

5) 'For all four tunneling-spectroscopy devices (1, 3, 4 and 5) the zeroth lobe, where the winding number is 0, shows a hard gap and no subgap states are visible.' SOM p3, commenting on all devices.

6) 'For device 5, a discrete state crosses zero-energy around  $VBG = 0.12$  V and then again at  $0.17$  V, resembling a proximitized quantum dot state, similar to the one previously studied in Ref. [84], see Fig. S7. We usually associate such state with a resonant level in the barrier and if possible avoid it in the measurements.' SOM p3, commenting on device 5.

7) 'The zeroth lobe shows a hard superconducting gap,...' Fig S6, commenting on data from Device 4

8) *'The zeroth lobe shows a hard superconducting gap,...'* Fig S7, commenting on data from Device 5.

#### A.3 On tunneling spectroscopy within the first lobe of the Little-Parks oscillations

1) *'In the superconducting regions around one quantum of applied flux, corresponding to phase twists of  $\pm 2\pi$  in the shell, tunneling spectra into the core show stable zero-bias peaks, indicating a discrete subgap state fixed at zero energy.'* Research Article Summary.

2) *'Upon reopening, a narrow zero-bias conductance peak was observed throughout the first gapped lobe (Fig. 2, B and F). Several flux-dependent subgap states are also visible, separated from the zero-bias peak in the first lobe.'* Research Article Summary.

3) *'In the first lobe, at  $B = 110$  mT, the sweep of VBG showed a zero-energy state throughout the tunneling regime (Fig. 2E). The cut displayed in Fig. 2F shows a discrete zero-bias peak separated from other states by a softened gap, presumably owing to finite temperature and level broadening in the junction. As the tunnel barrier is opened, the zero-bias peak gradually evolves into a zero-bias dip.'* p2.

4) *'...the first lobes show a zero-bias peak,...'* Fig. 2, commenting on data from Device 1.

5) *'In the first lobe, with the phase winding of  $2\pi$ , the spectrum for devices 1, 3 and 4 (all with 30 nm Al shell) displays a discrete, zero-energy state (see main-text Fig. 2, and Figs. S5 and S6),...'* – SOM p3, commenting on data from devices 1, 3 and 4.

6) *'...the first lobe shows zero-bias peak,...'* Fig. S5, commenting on data from device 3.

7) *'...the first lobes show subgap states including a zero-bias peak,...'* – Fig. S6, commenting on data from device 4.

#### A.4 On tunneling spectroscopy within the second lobe of the Little-Parks oscillations:

1) *'A second gapped lobe centered around  $|B| = 220$  mT then appeared, containing several subgap states away from zero energy...'* p2, commenting on data from Device 1.

2) *'...and the second lobes show nonzero subgap states.'* Fig. 2, commenting on data from Device 1.

3) *'In the second lobe, with even number of phase windings, the spectrum for device 1 features an asymmetric superconducting density of states with the lowest energy subgap state centered around ~5 eV, see Fig. S3; For devices 3 and 4, multiple subgap states can be identified at finite voltage, but no zero-bias peak, see Figs. S5 and S6; For device 5, a qualitatively similar to the first lobe spectrum with several finite-energy states is observed, see Fig. S7.'* SOM p3, commenting on all devices.

4) *'The spectrum shows subgap states away from zero energy.'* Fig. S3, commenting on data from Device 1.

5) *'...the second lobe shows non-zero energy subgap states.'* Fig. S5, commenting on data from Device 3.

6) *'...the second lobes show non-zero energy subgap states.'* Fig. S6, commenting on data from Device 5.

7) *'...the higher-order lobes show multiple discrete states away from zero energy.'* Fig. S7, commenting on data from device 5, *'...higher-order lobes...'* meaning first lobe and onward.

A.5 On tunneling spectroscopy within the third lobe of the Little-Parks oscillations:

1) *'Device 4 with slightly bigger diameter, displays the third lobe, with odd number of phase windings. The spectrum features subgap states and a peak at zero bias, see Fig. S6.'* SOM p3, commenting on data from Device 4, the only device shown with a third lobe.

2) *'The third lobes show subgap states again with a peak at zero bias.'* Fig. S6, commenting on data from Device 4.

A.6 On device 5 where no ZBP was shown (some quotes already included earlier):

1) *'In the first lobe, with the phase winding of  $2\pi$ ,... ...for device 5 (with 10 nm Al shell) the spectrum consists of multiple discrete, but finite energy subgap states, see Fig. S7.'* SOM text p3, commenting on device 5.

2) *'For device 5, a qualitatively similar to the first lobe spectrum with several finite-energy states is observed, see Fig. S7.'* SOM text p3, commenting on tunnelling spectroscopy in the second lobe for device 5.

3) *'For device 5, a discrete state crosses zero-energy around VBG = 0.12 V and then again at 0.17 V, resembling a proximitized quantum dot state, similar to the one previously studied in Ref. [84], see Fig. S7. We usually associate such state with a resonant level in the barrier and if possible avoid it in the measurements.'* SOM text p3, commenting on subgap resonances in device 5

4) *'Tunneling spectroscopy without zero-bias peaks in device with thinner Al shell (device 5).'* Fig. S7, caption title.

5) *'The zeroth lobe shows a hard superconducting gap, the higher-order lobes show multiple discrete states away from zero energy. No destructive regime is present in the thinner-shell device.'* Fig. S7, commenting on data from device 5.

6) *'...whereas for device 5 (with 10 nm Al shell) the spectrum consists of multiple discrete, but finite energy subgap states, see Fig. S7.'* SOM text p3, commenting on data from device 5 in comparison to devices 1,3,4.